12-3-2018

Investigation of the Viability of Thermographic Phosphor as a Sensing Mechanism for Structural Damage in Aerogel and PDMS

Katherine Elizabeth Mitchell

INVESTIGATION OF THE VIABILITY OF THERMOGRAPHIC PHOSPHOR AS A
SENSING MECHANISM FOR STRUCTURAL DAMAGE IN AEROGEL AND PDMS

by

Katherine Mitchell

A Thesis

Submitted in Partial Fulfillment of the

Requirements for the Degree of

Master of Science

Major: Physics

The University of Memphis

December 2018

Dedicated to those who supported me through this.

Acknowledgements

First, thank you to my advisor and mentor Dr. Firouzeh Sabri for all her support over these years. Also, thank you to my committee members Dr. Jingbiao Cui, Dr. M. Shah Jahan, and Dr. Xiao Shen. To Dr. Allison, thank you for your support in this study. Many thanks to all my lab mates. Thank you to my family. And thank you to Tim.

Abstract

Detecting structural damage in a material before complete failure has been a challenge with respect to material access, sensing mechanism resolution, and environmental setting, among other factors. In this work, the feasibility of using thermographic phosphors as a non-contact, instantaneous, and customizable sensing mechanism for detection of structural damage was investigated. The two materials were (1) Sylgard 184 elastomer and (2) silica aerogels. Both materials were impregnated with thermographic phosphors using different methods and tested over a wide range of temperatures. The degree of fracture in either material was gradually increased to represent a complete material failure scenario and a gradual propagation of defect that has not yet led to ultimate failure. The aerogel synthesis methodology was optimized for phosphor application so that either a discrete layer of phosphor would be embedded or a homogeneous mix was created and phosphor was distributed uniformly throughout the material. The discreteness of the phosphor layer was identified by two distinct points representing the entrance and exit points of the excitation and emission beams. The composite materials (homogeneous and otherwise) were fully characterized, and the sensitivity of the remote, non-contact sensing was evaluated. It was determined that fracture and failure in both aerogel and PDMS could be detected by phosphor thermometry and the limit of its resolution was ultimately determined by the thermal properties of the material, the choice of phosphors, and ambient temperature. In conclusion, thermographic phosphor powders were successfully incorporated at discrete levels and superficially in aerogels and in PDMS materials and as a result can be used as means to interrogate the bulk of the material. Phosphor thermometry proved to be a

viable option for remotely identifying structural defects in these two materials, with

limitations. The changes in the thermal profile of the material as a result of material

defects were used to infer information about the structural health of the material.

Table of Contents

List of Tables

List of Figures

Chapter 1

Introduction

This investigation focuses on the feasibility study of using phosphor thermometry as means to interrogate materials superficially and in-depth, for signs of wear, fatigue, and material failure. The two materials chosen for this study serve many industries and are widely used for insulation, encapsulation, and protection, under extreme conditions and as a result are subject to wear and accelerating aging. One of the materials chosen is the mesoporous material - aerogel - widely recognized for its superior insulative properties, and the other material is a biostable, biocompatible, transparent, and highly versatile elastomer, commercially available as Sylgard 184 (Dow Corning). This chapter provides an overview of the motivation behind this work and the methodology we adopted.

1.1 Aerogels and Their Properties

Aerogels were first synthesized in 1932 by Kistler and have since become a topic of significant research interest due to the unique properties that these materials have (1). Aerogels can be made from a variety of precursors using the sol-gel method and can be designed to be opaque, transparent, flexible, or stiff (1). The key material property that makes aerogels superior to many other material types is the highly porous structure of the material, often quoted to be as high as 90%, for some formulations (2). The high demand for better insulators that will continue to perform in extreme conditions without adding

significant weight has made aerogels an important discovery. Aerogels have been used for aerospace applications from NASA's Stardust Probe (3), the Mars Rover (2), and Space Shuttle (4) to applications in insulation in cold weather gear (5), building applications (6), and more recently in biomedical applications as a nerve regeneration scaffold (7). The continuous research investment in aerogels has allowed aerogels to replace conventional materials in some cases (8). As mentioned previously, aerogels have been reported to have porosities as high as 90% (9), densities as low as 0.003 g/cc (10), and thermal conductivities as low as 0.013 W/mK (6). It is the combination of these properties, not seen in other classes of materials, that has made aerogels a highly sought after material particularly for insulative applications (11), (12), (13), (14), (15).

Among the different types of aerogels, silica-based aerogels (crosslinked and other) are among those that have been studied the most (1). Chemically, the skeletal nanoparticles of silica aerogels are constructed of amorphous silicon dioxide (2) which creates a pearl necklace network (1). The synthesis process of aerogels in general allows for fine-tuning of surface and bulk properties to meet the needs and expectations of the intended use (1), (16), (17). Research in improving aerogel properties and designing new formulations is on-going and continues to grow.

1.2 Sylgard 184 Elastomer

Polydimethylsiloxane (PDMS) compounds, commonly referred to as silicones, are highly versatile elastomers that are mostly inert, non-toxic, and non-flammable (18), (19), (20). They are also transparent in the visible range and as a result well-suited for design of optical devices and flexible sensors/electronics. These materials are also popular for encapsulating purposes because of their thermal and electrical properties and are used in

many industries. Their applications range from microelectronics, to biomedical devices, to aerospace (18), (19), (20), (21), (22), (23). As a result, they are often exposed to extreme environmental conditions which can lead to material failure and degradation, prematurely. One of the most popular silicones is Sylgard-184 manufactured by Dow Corning and is one of the materials chosen for this study.

1.3 Structural Damage in Materials

Since World War II, research to understand material failure and prevention of such has advanced significantly. In the 1980s, a study was performed which estimated $119 billion per year as the cost resulting from material failure due to fracture specifically – $311 billion in 2018 dollars (24). This highlights and emphasizes the need for mechanism and technologies that can assist us with early detection of material damage before failure occurs. Fracture in materials can occur for a number of reasons, including simple tensile overstress (25), (26). Material failure often occurs at the end of a material's lifetime, though the specific criterion that define failure are not widely agreed upon (27). Failure can occur due to fracture, total disintegration, change of shape, or change in mechanical properties, among others (28). There are over 20 distinct phenomena that can cause a material to fail. Among the most commonly studied causes: fracture, fatigue, wear, and corrosion – fracture (28) was chosen as the mechanical damage mechanism for this investigation. Existing methods for detection of fracture or cracks in a material cannot be used in all cases, or environments, and have limited resolution (29). For insulative materials, cracks can result in full or partial loss of the thermal integrity of the material which can lead to catastrophic loss including loss of life in some applications (30), (31). A commonly-used method for detection of structural

damage and analysis used today is ultrasound detection. Ultrasound technology can

remotely detect structural damage in materials (32) such as concrete (32), (33), pipes

(34), or metal railways (35). However, the nature of this technique severely limits its

range of applicability and the resolution it can deliver (36). Therefore, there is an urgent

need for new technologies and methods for detecting material fracture(s) using

technologies and principles other than ultrasound, and is the focus of this investigation.

This research has focused on exploring mechanisms to monitor temperature profile of the

intended material to infer structural damage concerns. This is particularly important for

insulative materials where the insulation performance of the material can be severely

compromised due to the presence and propagation of defects. Existing methods used for

temperature detection such as thermocouples (37), thermal paints (38), and pyrometry

(39) are not suitable for all materials and applications. For example, thermocouples

require direct contact, time for the sensing tip to reach thermal equilibrium with the

material being measured, and have a range limited by the constraints of the instruments

such as the wire diameter (40). Direct contact is not necessarily available in extreme

environments such as space or an environment with a complex geometry such as a

rotating turbine (41), (42). Thermal paints must be applied to a surface irreversibly,

which is invasive and could damage sensitive material (29). Pyrometry is a remote

method of temperature sensing, but the emissivity of the surface is required which is not

always available and changes as the surface temperature changes (43). One the other

hand, thermographic phosphors are an attractive alternative option in lieu of the

shortcomings in these temperature detecting mechanisms. Phosphor thermometry is a

remote, precise, and non-invasive technique and is further discussed later in the document

(44). This work investigates the feasibility of using thermographic phosphor as a remote sensing mechanism to identify structural damage and defects in aerogels and PDMS.

1.4 Phosphor Thermometry for Non-Contact Sensing

Thermographic phosphors have properties that change based on temperature when excited by a source light (45). Analyzing these properties to determine the temperature of the phosphor provides information about the temperature of the phosphor and the surface it is in contact with. If a temperature gradient is present, the properties of the phosphor will change with the temperature gradient. If the phosphor is present on or in an insulative material that has been compromised, a temperature gradient due to the structural damage may be detectable by the changes in phosphor properties such as decay time. This mechanism is functional under extreme temperature. Some phosphors are sensitive at temperatures as low as cryogenic temperatures up to 1700°C with a precision as low as 0.05°C (36). Also because the phosphor's mechanism is remote and light based, this mechanism is usable in extreme conditions such as under vacuum or in combustion environments. The Luminescent emission is independent of electromagnetic interference or other external triggers (46). This measurement method enlists an instantaneous optical system, which is independent of emissivity, unlike pyrometry. This technique could provide a more elegant and precise method to identify loss of structural integrity for this category of materials.

1.5 Research Aims

The scope of this study included developing a synthesis protocol for incorporating phosphor into aerogel synthesis as a discretely embedded layer, developing a repeatable,

controllable damage protocol for both aerogel and PDMS, and determining the feasibility of thermographic phosphor as a damage sensing mechanism in aerogel and PDMS.

1.6 Thesis Outline

Chapter 2 discusses the theory of luminescence, phosphor thermometry, UV-Visible spectroscopy, and thermal conductivity. Chapter 3 contains the methods of sample synthesis, characterization, and experimentation. Chapter 4 presents the results and discussion of this research. Chapter 5 concludes this research and suggests future work.

Chapter 2

Theoretical Background

2.1 Introduction to Heat Transfer

Heat is defined as a measure of the change in the total kinetic energy of a substance (47) and is proportional to the average kinetic energy, independent of the size of the object or substance (47). In general, heat transfer can be described by Equation 1,

$$\nabla q + \Phi = \rho c \frac{dT}{dt} \tag{1}$$

where q is heat flux density, Φ is radiative heat flux density, ρ is density, c is specific heat, T is local temperature, and t is time (1). There are 3 types of heat transfer: conduction, convection, and radiation (48). Convection is described as heat transfer through a moving fluid from a boundary surface to a fluid (49). Newton's law of cooling, Equation 2, describes the relationship between heat transferred from a body to a fluid and the change in temperature between the surface temperature and fluid temperature,

$$q'' = h(T_w - T_f) \tag{2}$$

where q" is heat flux (heat per area), h is a heat transfer coefficient, T_w is the surface temperature, and T_f is the characteristic fluid temperature. The heat transfer coefficient h may depend on the temperature difference in special cases (48). If the fluid is unbounded, T_f can be written as T_{inf}. This substitution suggests that the energy is replaced in the body

so its temperature does not change. The thermal resistance to heat lost by convection at the surface-fluid boundary is described by Equation 3,

$$R_{th} = \frac{1}{hA} \qquad (3)$$

where R_{th} is the thermal resistance, h is the heat transfer coefficient, and A is area (48). This suggests that increasing surface area or h will increase the time it takes a body to decrease in temperature. Conduction is the mode of heat transfer through solid material. Heat transfer via conduction is a result of microscopic energy carriers like molecules, free electrons, and phonons moving from a location of higher temperature to a location in physical contact at a lower temperature (49). The conductive thermal resistance can be calculated in a similar manner to Equation 3 by replacing the heat transfer coefficient with thermal conductivity per thickness (k/L) (48). Heat transfer via radiation occurs when energy is transferred through matter and does not require contact. The modified Stefan-Boltzmann law, Equation 4, relates temperature to energy radiation in terms of emissivity and the Stefan-Boltzmann constant on a macroscopic level,

$$e = \varepsilon \sigma T^4 \qquad (4)$$

where e is the energy flux emitted by a radiator, ε is the emissivity, σ is the Stefan-Boltzmann constant, and T is temperature (48).

2.1.1 Heat Propagation in Aerogels

Heat propagation in porous material such as aerogel occurs via all three modes in combination as shown by the cartoon in Figure 1. Equation 1 can be applied to porous

8

materials and therefore aerogel. For isotropic material with heat transfer depending only on local temperature gradient, Equation 1 can be simplified to Equation 5,

$$\Delta T = \frac{1}{a} \frac{\delta T}{\delta t} \tag{5}$$

where a is thermal diffusivity $a = \frac{\lambda}{\rho c}$ and ρc the volumetric specific heat, relevant to nonstationary heat transfer where temperature and heat flux changes with time (1). As shown in Figure 1, contact-based heat transfer through aerogel occurs in two manners, gaseous heat conduction and solid heat conduction, due to the aerogel being composed of both a solid matrix and pore structure filled with gas (9). Aerogel conducts heat poorly because the mean free path of gas atoms moving through the pores of the material at standard temperature and pressure is approximately 69 nm (9) while the aerogel pores are smaller, with published averages ranging from 20-40 nm (1). The small pores restrict the movement of gas through the material, reducing gaseous heat conduction. The restriction of solid heat conduction occurs in a parallel manner. The average particle diameter vibrating in the lattice is 2-5 nm as reported in literature (50), and the mean free path of phonons is approximately 0.58 nm (51). The phonons are challenged to move through the solid aerogel matrix due to the closeness in size, reducing the thermal conductivity (52). The low density of aerogel and complex internal structure also lengthens the mean free path of the phonons and further reduces the heat transfer (9). If crack or fracture occurs in aerogel, the convection of heat would be magnified because the void size would increase from approximately 20 nm to the size of the damage. The heat flow restriction would decrease, increasing the thermal conductivity at that location. With respect to thermal radiation, aerogel has a small absorption coefficient, and consequently high transparency,

for wavelengths between 3 and 8 μm, which falls in the IR region of light. As a result, at increasing temperatures, aerogel experiences an increase in thermal conductivity and transfers radiative heat more readily (53). This radiative behavior results in an upper limit of temperature in which aerogel remains healthy and beneficial for insulative applications.
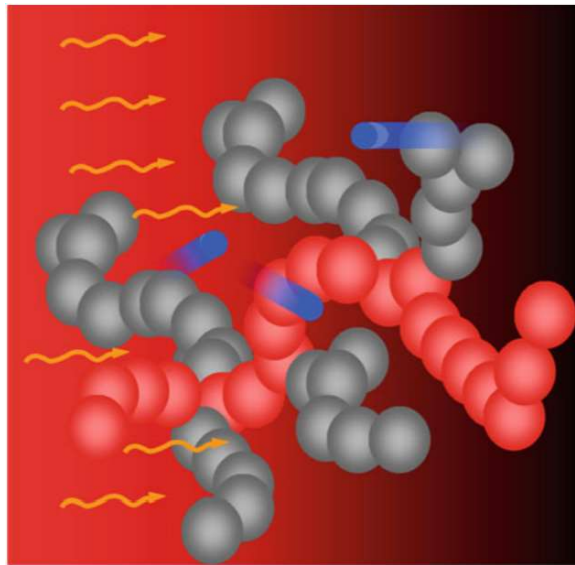
Figure 1: The red and grey spheres represent the solid aerogel internal network, where the red spheres are undergoing conductive heat transfer. Convection occurs through the voids of the porous structure as indicated by the blue spheres. And radiation is represented by the yellow arrows, independent of heat source contact (1).

2.2 Thermal Conductivity

Thermal conductivity is defined as the constant of proportionality between heat flux and temperature gradient, as expressed in Equation 6 (54):

$$q = -k\frac{dT}{dx} \tag{6}$$

Structure, density, and porosity all intrinsically affect the thermal conductivity of a material, as discussed in Section 2.1 (55). Thermal conductivity for a given material will also change with the temperature of the material (56). There are a variety of methods for measuring thermal conductivity depending on sample thickness and approach. Three commonly used approaches for measuring thermal conductivity are steady-state, frequency-domain transient, and time-domain transient techniques (57). Transient plane source, a time-domain transient method was used to measure the thermal conductivity of samples in this work because it was the measuring mechanism of the Therm Test instrument used in this study.

2.2.1 Transient Plane Source

This research used a transient plane source (TPS) technique to measure thermal conductivity (58). The TPS method uses a hot disk sensor with a double spiral of electrically conductive nickel, as pictured in Figure 2 (59), between two sheets of Kapton insulation (55), (59). Identical and sufficiently large samples are placed on either side of the sensor. As direct current passed through the sensor, the sensor temperature increases via resistive heating. The temperature increase typically ranges from 0.4-4 K. As the resistance increases, a corresponding voltage drop occurs. The resistance increase, R(t), with time can be modeled as follows starting from Equation 7,

$$R(t) = R_o\big[1 + \alpha\{\Delta T_o + \Delta T_{avg}(\tau)\}\big] \qquad (7)$$

where R_o is the resistance of the disk just before heating, ΔT_o is constant temperature difference between the thin insulating layers covering each side of the nickel sensor, $\Delta T_{avg}(\tau)$ is the temperature increase on the sample surface, and α is the temperature

coefficient of the resistivity. From Equation 7, the temperature change can be written as Equation 8, where the sensor records the temperature increase $\Delta T_{avg}(t)$,

$$\Delta T_{avg}(t) + \Delta T_o = \frac{1}{\alpha}\left(\frac{R(t)}{R_o} - 1\right) \tag{8}$$

The total change in temperature can then be written as Equation 9,

$$\Delta T_t(t) = \Delta T_o + \Delta T_{avg}(t) \tag{9}$$

The changes in voltage, current, and temperature over time produce heat flow information (59). A plot of temperature increase versus time is extracted, and the slope of the linear portion of the plot is calculated and used to calculate thermal conductivity with Equation 10,

$$k = \frac{P}{\pi^{3/2} am} \tag{10}$$

where k is thermal conductivity, P is power, a is sensor radius, and m is the slope of temperature increase vs. time (59).
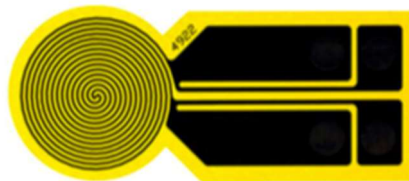
Figure 2: Kapton Hot Disk sensor used for thermal conductivity measurements (59).

The TPS theoretical model was based on several assumptions. In order for measured values to be precise, several parameters must be properly chosen to reduce measurement error including disk size, test duration, sample size, and power level (55).

The TPS model assumes that the measured sample was infinite, isotropic, and homogenous. Therefore, the measurements were made on isotropic and homogeneous sample, and the samples measured were of sufficient thickness and diameter with the appropriately corresponding sensor disk diameter, per recommendation by the equipment manufacturer (59). In this study, because the materials measured were expected to have a relatively low thermal conductivity, a maximum power limit of 20 mW was selected as recommended by the equipment manufacturer Therm Test (59). The theory also assumed that the sensor has negligible thickness and heat capacity as well as negligible thermal resistance between the sensor and sample. These assumptions lead to sources of error in TPS measurements because the sensor's linear electrical sources are placed in equally spaced concentric circles, the input power is increased in discrete steps, and there is a small and difficult to quantify loss of heat input intended to flow through the sample (60), (61). This loss of heat can stem from the sensor not being in full contact with the sample surface and the fact that the sensor does indeed have a thickness and heat capacity, no matter how small.

2.3 Evaluation of Material Failure

An important material property that is often affected adversely by material failure, fatigue, and aging is the material's Young's modulus as described by Equation 11,

$$E = \frac{\sigma}{\varepsilon} \tag{11}$$

where E is the Young's modulus, σ is the stress applied, and ε is the strain deformation (62). The type of defect and aging-related material failure can take on a variety of forms.

This work focuses on mechanical failure as a result of crack propagation or fracture. Strain energy S, shown by Equation 12, and surface energy U, shown by Equation 13, are functions of crack length, a, at the edge of a material due to tensile stress, σ:

$$U = -\frac{\sigma^2}{2E}\pi a^2 \tag{12}$$

$$S = 2\gamma a \tag{13}$$

where γ is surface energy and the constant 2 is required due to the formation of 2 surfaces at the crack (24). At a critical length, a previously-formed crack can propagate through the entire material resulting in complete material failure. The critical crack length occurs when the derivate of S+U is 0, as shown by Equation 14,

$$\frac{\delta(S + U)}{\delta a} = 2\gamma + \frac{\sigma_f^2}{E}\pi a = 0 \tag{14}$$

The stress required for catastrophic failure to occur when a crack reaches critical length, solved for by manipulating Equation 14, is shown by Equation 15:

$$\sigma_f = \sqrt{\frac{2E\gamma}{\pi a}} \tag{15}$$

However, Equation W was derived by assuming that the material is brittle. When the material is ductile, the surface energy alone is not enough to describe crack behavior (24). Therefore, a critical strain energy release rate, G_c, was introduced to account for the other energy sinks in the material when cracking occurs. This correction can be shown by Equation 16:

$$\sigma_f = \sqrt{\frac{EG_c}{\pi a}} \tag{16}$$

Equation 16 concisely summarizes the relationship between the material properties, stress, and flaw size (24). With respect to compressive forces, under hydrostatic pressure the volume of a solid reduces and this phenomenon is referred to as dilation or volume strain, defined by Equation 17 (25),

$$\varepsilon_{kk} = \frac{\Delta V}{V} \tag{17}$$

This is related to applied pressure by the bulk modulus, Equation 18 (25):

$$p = -K\varepsilon_{kk} \tag{18}$$

The relationship between cracks in a material and the thermal conductivity of the same material can be modeled by assuming the crack is a flat pore of ellipsoidal geometry with the minor axis approaching zero. This model applies as long as the crack under investigation is a small fraction of the entire material volume and radiative or convective heat transfer across the cracks are absent (30). A general solution proposed for the thermal conductivity of a material containing uniformly dispersed cracks, each with zero thermal conductivity, is presented as Equations 19 and 20,

$$K = K_o - \frac{V}{1-V} \sum_i^{i=a,b,c} \frac{2K}{2 - abcL_i} \tag{19}$$

where

$$L_i = \frac{2A_i}{abc} \tag{20}$$

and K_o is the thermal conductivity of the material matrix, a, b, and c are the ellipsoid axis, and V is the volume fraction of the dispersed phase (30). For randomly oriented cracks distributed uniformly throughout the matrix, thermal conductivity can be written in terms of crack size and density for N number of cracks as Equation 21 derived from Equation 19 (30),

$$K = K_o \left(1 + \frac{8Nb^3}{9} \right)^{-1} \tag{21}$$

Further investigation is required to determine the specific limitations of this model. Computational work was outside the scope of this investigation but is of interest to the author and her research group.

2.4 Phosphor Thermometry

Luminescence is a form of radiation not derived from heat, unlike blackbody radiation or incandescence (63). It occurs when an electron is excited to a higher energy level and then releases energy in the form of light emission (64). Different forms of luminescence include chemoluminescnece, electroluminescence, bioluminescence, and photoluminescence (65). Photoluminescence is the focus of this research due to light energy of the phosphor being the source of luminescence emission (66). This luminescent emission is independent of electromagnetic interference or other external triggers (67).

Photoluminescence can be broken into 2 categories: fluorescence and phosphorescence. Phosphorescence has a longer lifetime, up to 10^{-3} s, than fluorescence which lasts up to 10^{-9} s (68). When an electron is excited from its ground state, it jumps up to a higher energy level. As it relaxes back toward the ground state, it releases energy

16

which can be seen as luminescent light. If the electron follows the path of fluorescence, it

falls straight back to the ground state during transition. However, during

phosphorescence the electron first transitions down to a triplet state in which its spin

reverses. This is called the forbidden triplet state (66), (69). This forbidden state exists in

the forbidden band gap between the valence and conduction bands (64), (70). The

transition back to the ground state from the forbidden triplet state is much slower because

the electron must again reverse spin in order to follow the Pauli exclusion principal in the

ground state (43). This is why phosphorescence has a longer decay lifetime than

fluorescence. Photoluminescent excitation and decay pathways can be described visually

by a Jablonski energy diagram as shown in Figure 3 (71).
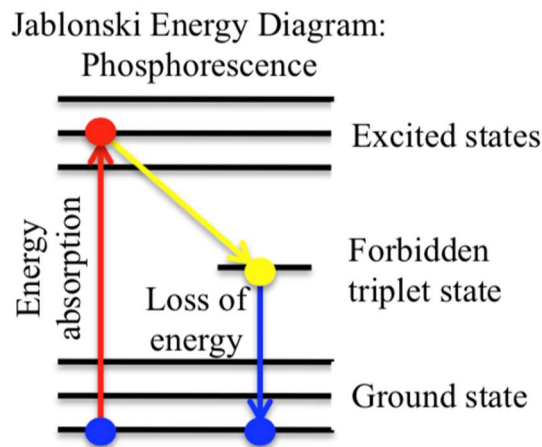
Figure 3: Jablonski energy diagram showing the phosphorescent path of an electron's
excitation and decay

Phosphor thermometry employs thermographic phosphors as a temperature

sensing mechanism. Generally thermographic phosphors are phosphorescent (66).

Thermographic phosphors have at least one aspect of their luminescent emission that is

temperature dependent, making them ideal for applications in this research (46).

Phosphor thermometry is a remote and noninvasive process that can be used over a wide

range of temperatures and is highly versatile (66), (67), (64), (72), (45).

2.4.1 Thermographic Phosphors

Thermographic phosphors are typically made of a metal oxide doped with a rare

earth ion or oxysulfide. A host material makes up the lattice structure of the phosphor

compound. Halides, oxides, and oxysulfides are common host materials. La_2O_2S is an

oxysulfide host; $Mg_3F_2GeO_4$ is a halide-based lattice (73). Defects, like rare-earth ions,

can be added to phosphor compounds to alter the luminescent properties. These defects

can also be transition metal ions like Mn^{2+}, actinides, and heavy metals (70). The dopant

ion is the part of the compound that absorbs and emits the photons (73). The

concentration of activator dopant affects the decay time and emission intensity (66).

Dopant concentration, characteristic size of phosphor particles when smaller than 5

microns, impurities, and magnetic field at very cold temperatures all affect luminescent

properties of a compound (74).

In the case of europium-doped lanthanum oxysulfide (La_2O_2S:Eu), Eu^{3+} is a rare

earth ion that behaves as an activator. Lanthanide ions (Eu^{3+}) have an incomplete 4f shell,

so as a low concentration dopant in a host lattice, it acts as a free ion (66). The La_2O_2S:Eu

used in this study had a 1% dopant concentration. La_2O_2S:Eu is sensitive to 0.05°C, with

bands that have temperature dependent decay times from cryogenic temperatures to

600K. The 538 nm emission band has a temperature sensitive decay time between 350K

and 625K, and the 512 nm band has an upper boundary of temperature sensitive decay

time around room temperature (75). The other phosphor powder studied in this work was magnesium fluorogermanate doped with manganese ($Mg_3F_2GeO_4$:Mn) which is sensitive to <1°C. $Mg_3F_2GeO_4$:Mn has temperature dependent electron bands from 8K to 1070 K (76).

The phosphors that can be excited and emit at longer wavelengths will have less absorption and scattering, which is discussed further in Section 2.8. The wavelength of the emission depends on the difference in energy of the ground state and excitation state (70). The gap between the valence and conduction bands is defined as the forbidden band as depicted in Figure 4 (64). The amount of energy needed for an electron to jump from the valence band to the conduction band is described by Equation 22,

$$E = h\nu \tag{22}$$

where E is energy, h is Planck's constant, and ν is frequency (64).
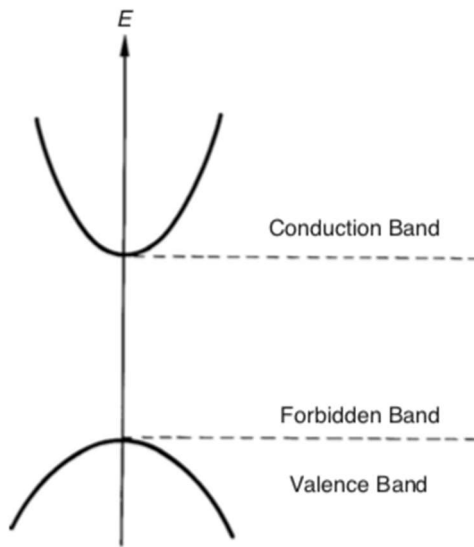
Figure 4: Diagram of conduction, forbidden, and valence energy bands (64).

Various characteristics of thermographic phosphors that are affected by temperature include decay time, line shift and broadening, intensity of emission, emission distribution, absorption band width and position, excitation band width and position (77), (69). However, not every characteristic is temperature dependent or strongly temperature dependent in every type of phosphor, for all temperature ranges. The two types of phosphors used in this study were La_2O_2S:Eu and $Mg_3F_2GeO_4$:Mn, and in both cases their decay time was temperature dependent.

2.4.2 Decay Time Analysis

The lifetime of luminescent emission can be defined by the intensity of emission, time, and decay constant as related by Equation 23,

$$I = I_o e^{-t/\tau} \tag{23}$$

where I is intensity proportional to the population in the state, I_o is the intensity at t = 0, and τ is the decay time (67). The decay time describes the time needed to diminish the total intensity by a factor of 1/e (76). The decay time τ_q, time constant τ_d, and temperature T are related by Equation 24,

$$\tau_d = \tau_q e^{-Q(T-T_Q)} \tag{24}$$

where Q is the quenching rate (the rate when the decay time varies with temperature) and T_Q is the quenching point (67).

Decay time τ and temperature are related by a set of constants dependent on the emission band. The relationship is derived experimentally and shown in Equation 25 (78):

$$\tau = \left(\frac{1}{\tau_o} + ae^{-\Delta E/(kT)}\right)^{-1} \tag{25}$$

This relationship is dependent on dopant concentration and is affected by particle size and impurities (78).

2.5 UV-Visible Spectroscopy

Light interacting with a material can be separated based on the material properties. In general, light is absorbed, reflected, or transmitted (79). These optical properties of a material are affected by many factors including internal structure, color, surface roughness, homogeneity, and composition, among others (80).

2.5.1 Transmittance

Transmitted light is that which passed through a material. There are two types of transmitted light, as shown in Figure 5a: direct and diffuse. Direct transmission passes through the material at an unaltered angle, while diffuse transmission is a type of scattering that occurs when light passed through the material changes angle either in the material or on the back surface of the material, where scattering is defined as a redirection of light in any direction than that of the incident angle (79). Diffuse transmission is a result of refraction in a material because the index of the source medium is different than that of the material medium (79).

2.5.2 Absorbance

The Beer-Lambert law, shown in Equation 26, identifies the basic relationship between absorbance and material characteristics, extinction coefficient, thickness, and concentration (81),

$$A = \varepsilon b c \tag{26}$$

where A is absorbance, ε is molar absorption (extinction coefficient), b is path length (thickness), and c is concentration of absorbing species. Absorbance is measured with a spectrophotometer by collecting the amount of directly transmitted light T and calculated with Equation 27 (82),

$$A = \log\left(\frac{1}{T}\right) \tag{27}$$

This metric contains error in that it is actually the absorbed light as well as any reflected light and light scattered as diffuse transmission. A more accurate description of this metric is attenuance (83). Therefore, to calculate attenuance both reflectance and transmittance were measured and subtracted from the total incident light.

2.5.3 Reflectance

Reflectance occurs when light incident to a surface reaches the surface of the material and is scattered backward (84), (85). There are two types of reflectance, as shown in Figure 5b: specular, where the incident beam is reflected at the same angle of the angle of incidence, and diffuse, where the incident beam can be reflected in any

direction (86). An integrating sphere can be used to measure diffuse reflectance while other special attachments are needed to measure specular reflectance (82).
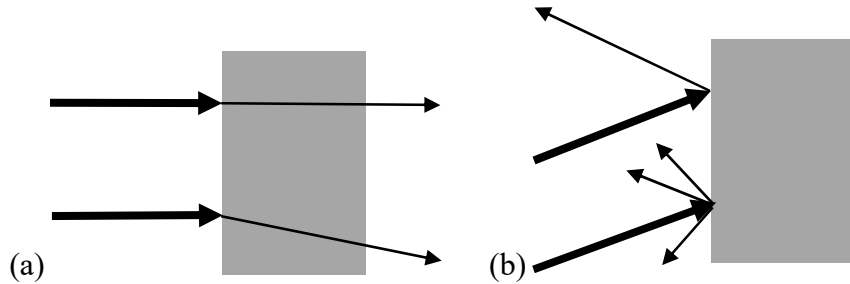
Figure 5: Schematic depicting the differences in specular (or direct) and diffuse (a) transmittance and (b) reflectance

The Rayleigh-Gans theory is one model that was created to separate the effects of scattering and absorption, as described by Equation 28 (87),

$$T = Ae^{-Bt/\lambda^4} \tag{28}$$

where T is % transmission, λ is wavelength, t is sample thickness, A and B are constants called Hunt parameters (88). According to this theory, absorption is dominant over scattering at longer wavelengths, but scattering is more important in the UV-visible range (88). Rayleigh scattering describes the intensity of scattered light as proportional to λ^{-4} and occurs when particles are much smaller than the wavelength (79). Equation 28 takes into account surface defects and large features with the wavelength independent constant A and the internal structure of the material is accounted for by the constant B, the extinction contribution from Rayleigh scattering. B is limited to describing the scattering in the region of the spectrum where scattering is dominant. This equation is based on the Beer-Lambert Law, which limits it to describing propagation in one direction.

The average pore size for the aerogel is 3-4 orders of magnitude less than the wavelengths of UV-visible light. Because the particles are much smaller than the incident wavelength, Rayleigh scattering can be considered for aerogel. In the UV-visible range, reflectance intensity can be expected to be higher at the lower end wavelengths. Extrapolating from Equation 27, the transmittance will be related to reflection by the inverse exponential, meaning increasing the wavelength will also increase the percent transmission. Therefore, if a phosphor can be excited at a longer wavelength, it can be expected to have less absorption and scattering.

2.6 Drying and Reinforcing Aerogel

The drying step in the aerogel synthesis is the most sensitive step. Through the synthesis process, the sol-gel remains in solvents which occupy the future pore spaces. During the drying process, the solvent is removed leaving pores of air. If the solvent is not completely removed, the aerogel can have a reduction in clarity, increase in density, and even collapse (12). Using a critical point dryer, CPD, to dry aerogels consists of exchanging the solvent for liquid CO_2, raising the CO_2 to supercritical phase, and slowly outgassing the CO_2 to leave behind a dry, porous aerogel. CO_2 reaches its critical point at 31.1°C and 1071 psi, as shown in Figure 6 (89).

Crosslinker can be added to an aerogel to increase robustness (12). Native silica aerogel has a pearl necklace-like structure with large voids. It's weakest at the interface between the primary silica particles and secondary particles (12). A crosslinker reinforces the structure by adding covalent bonds and widening the interparticle necks where the structure is the weakest without a significant loss in porosity (90).
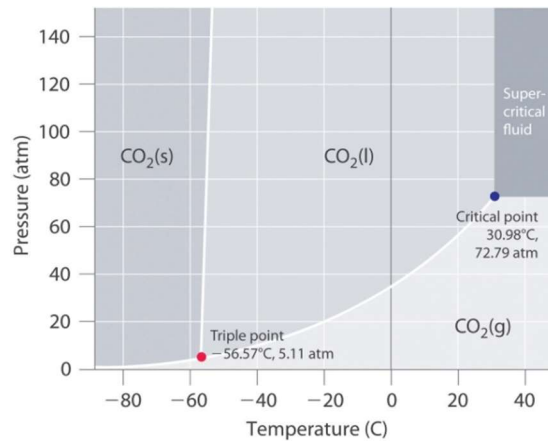
Figure 6: Phase diagram of CO_2 identifying the critical point at approximately 73 psi and 31°C (89).

Chapter 3

Methods

This chapter provides details of all the synthesis steps, and preparation of samples needed for this investigation. Crosslinked and non-crosslinked silica aerogels, and elastomeric samples were prepared and fully characterized. Details related to creating composite samples doped with thermographic phosphors have also been presented and described in detail.

3.1 Synthesis and Preparation of Samples

3.1.1 Non-crosslinked Silica Aerogels

A solution of 8.5 mL of methanol (Sigma Aldrich), 1.5 mL of deionized (DI) water, 3.85 mL of tetramethoxysiloxane (TMOS) (Sigma Aldrich), and 0.25 mL of 3-aminoproplysilane (ACROS Organics) was poured into previously-created custom silicone molds. The sol-gels were allowed to stand in the mold 3 hrs before being removed from the molds and placed into a methanol bath for 24 hrs. After 24 hrs, the methanol was removed and replaced with acetronitrile (Fisher Chemical). The aerogels were placed into 3 more subsequent acetonitrile baths each 24 hrs apart. The aerogels were then dried in a critical point dryer (CPD) model E3100-060 with liquid CO_2. Upon completion of the supercritical drying phase the aerogels were removed from the CPD and placed in a dessicator until further use. The density of each aerogel sample that was

prepared was calculated and documented for future use. At least 4 measurements were made from each sample and averaged. Three different thicknesses of non-crosslinked silica aerogels were made for this study. These were 2 mm, 5 mm, and 10 mm.

3.1.2 Crosslinked Silica Aerogels

The synthesis protocol described in Section 3.1.1 was modified to create crosslinked aerogels. Before the drying stage, to create crosslinked aerogels 33 gr of Desmodur N 3200A (Bayer) was dissolved in 94 mL of acetonitrile, and the samples were placed in this bath for 72 hrs in a Precision 3-M vacuum oven held at 70°C and under atmospheric pressure. After 72 hrs, the aerogels were placed in 3 consecutive acetonitrile baths for 24 hrs each. The aerogels were then dried in the same manner as described in the previous section. Density measurements were also made for each sample and documented. Crosslinked aerogels of 2 mm and 10 mm thicknesses were synthesized. The flow diagram shown in Figure 7 provides a summary of the steps followed to create crosslinked and non-crosslinked silica aerogels for this study.
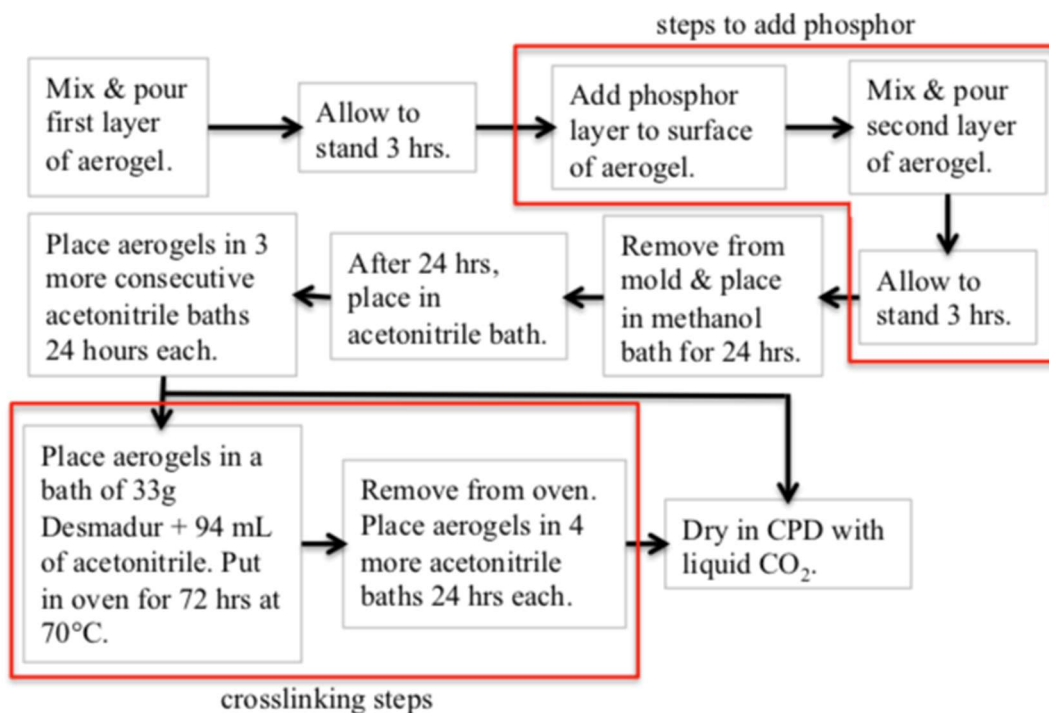
Figure 7: Flow diagram summarizing steps related to the synthesis of crosslinked and non-crosslinked silica aerogels, as well as aerogel-phosphor composites with varying layer structures to be discussed in Section 3.1.4.

3.1.3 Synthesis of Phosphor- Polydimethylsiloxane (PDMS) Composite Thin Films

Sylgard-184 (Dow Corning) elastomer was the other material chosen for this study. Sylgard-184 is a very versatile polymer that once crosslinked and cured, is very stable under extreme conditions both chemically and physically. Also, it is transparent in the visible range which makes it suitable for luminescence-related applications. It is also used frequently in a variety of applications as mentioned in Chapter 1. To synthesize the desired samples the base and crosslinker were mixed in a 10:1 ratio as recommended by the manufacturer. $La_2O_2S:Eu$ phosphor powder (Phosphor Technology SKL63/F-X lot

28

23010) was added by weight to reach the desired doping concentration. Samples of 10%, 25%, and 50% doping concentration were synthesized, and optical images of the fully cured samples are shown in Figure 8. The PDMS-phosphor slurry was mixed thoroughly and outgassed in a Precision 3-M vacuum oven at room temperature. The edges of an aluminum weigh boat (Fisher Scientific) were trimmed and the boat base was mounted on the stage of a Chemat Scientific spin coater. Approximately 2 mL of the slurry was poured onto the center of the plate and spun at 1000 rpm for 18 s. The optimum spin speed and spin time was determined experimentally, and a time of 18 s and speed of 1000 rpm gave rise to a thin but uniform film of reasonable thickness for this application, without being too thin to handle and was therefore chosen as the final spin conditions. The plate was then placed in the oven and cured at 100°C for 1 hr. Once cooled, the doped thin film was peeled from the aluminum substrate.
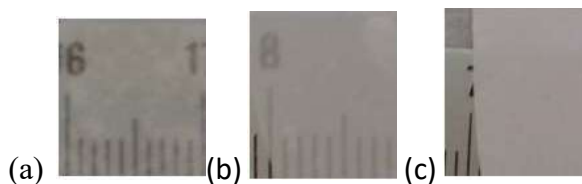
Figure 8: Optical images of La_2O_2S:Eu phosphor-doped PDMS thin films of dopant concentrations (a) 10%, (b) 25%, and (c) 50% used to identify 50% as the optimum dopant concentration for this work.

Microscopy imaging via an Accu-Scope Unitron microscope with an AmScope MU1000 Microscope Digital Camera was used to determine the phosphor cluster size and coverage of the La_2O_2S:Eu powder in PDMS thin films created by spin-coating. Images of each sample type were collected. Contrast in each image was manipulated with the AmScope software to increase the phosphor cluster shading and reduce the background

matrix shading. The images were then converted to binary color format, transforming the

shaded pixels of phosphor to black and the background PDMS to white. The percentage

of the black pixels the image within a calculated area was calculated to determine

approximate phosphor coverage. To calculate average cluster size, 25 measurements of

phosphor clusters were collected within an approximate 50 μm region and averaged. The

AmScope software was also used to collect the length measurements. Table 1 reports the

average phosphor cluster size and percentage of phosphor coverage, which provides

indications of the phosphor distribution throughout the material. Increasing the

percentage of phosphor concentration decreased the cluster diameter and increased the

phosphor coverage. As a result, 50% doped thin films were used in experimentation

because that condition resulted in the best phosphor dispersion through the PDMS.

Table 1: Cluster diameter and percent phosphor powder coverage of phosphor-doped
PDMS thin films with change in phosphor doping concentration based on microscope
image processing. It was determined that increasing the phosphor concentration decreases
average cluster diameter and increases percentage of phosphor coverage in the PDMS,
resulting in the selection of 50% doping concentration for this work.

Properties of 1000 rpm / 18 s Phosphor-doped PDMS Thin Films with Varying Dopant Concentration		
% Doping Concentration	Avg. Cluster Diameter (μm)	% Phosphor Coverage
10	12.01	57
25	7.23	74
50	4.35	87

3.1.4 Aerogel-Phosphor Composites

Three different configurations of crosslinked aerogel-phosphor composites identified by Method 1, Method 2 and Method 3 were synthesized and prepared for this study. A flow diagram detailing the layer structure(s) in each configuration is given in Figure 9.
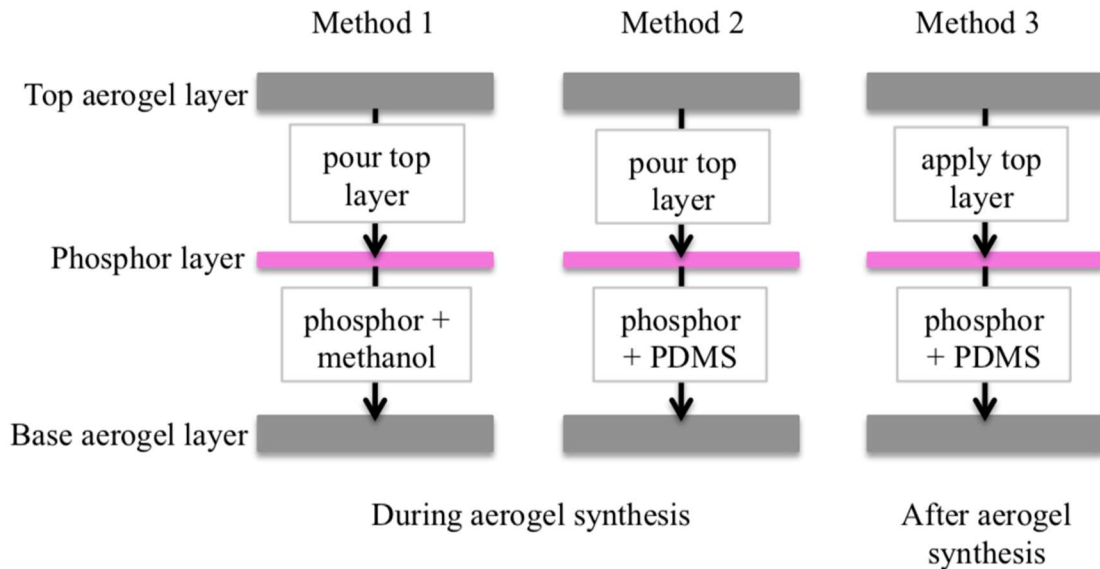
Figure 9: Schematic of 3 configurations used to synthesize aerogel-phosphor composites where Method 1 was selected for continued use for luminescent studies.

Two types of phosphor powder were used for synthesis of aerogel-phosphor composites: La_2O_2S:Eu and $Mg_3F_2GeO_4$:Mn (Phosphor Technology lot 23145). The La_2O_2S:Eu powder we used had a 1% Eu doping concentration. These specific phosphors were chosen because their decay behavior has a significant and detectable temperature dependence and therefore highly relevant to the goals of this study, as detailed in Chapter 2. The three different preparation methods are described in detail below:

Method 1. A layer of sol-gel solution prepared as described in Section 3.1.1 was poured into a silicone mold following the procedure previously described. It was allowed to set for 3 hrs. Phosphor powder and methanol were mixed in a 1:7 ratio by weight. 1 mL of the mixture was applied to the surface of the sol-gel in the mold, ensuring complete coverage of the sample surface. This was allowed to set for 1 hr while the methanol evaporated off the surface, leaving behind only a layer of evenly distributed phosphor powder. A cap layer of sol-gel solution was carefully poured onto the phosphor layer. The remaining steps to synthesize cross-linked aerogel were performed as described in Section 3.1.2.

In the CPD step, extra flushes were performed until the solvent was completely extracted from the CPD and the samples. The extra flushes were necessary because the phosphor impedes the solvent exchange. Even with best efforts, it was difficult to ensure the solvent had been fully flushed and replaced with CO_2. It was hypothesized that the non-crosslinked aerogel would have a more thorough solvent exchange than the crosslinked aerogel due to the absence of Desmodur. However, the non-crosslinked aerogel fractured during out gassing stage as seen in Figure 10a while the crosslinked aerogel remained intact as shown in Figures 10b and 10c. While the CPD stage was not perfect, allowing the samples to dry under atmospheric conditions was not an option due to severe surface tension effects and ultimately loss of pores of the aerogels. Figure 10d shows the effect of surface tension and clearly the aerogel disk shriveled and fractured rendering the sample non-usable.

Layering the phosphor into the aerogel during synthesis also presented many challenges. When pouring the cap layer of sol-gel solution over the phosphor layer, the

phosphor layer was disturbed at the location of the pour. This can be seen in Figures 10a and 10b where the phosphor is missing in the center of the sample. This problem was not mitigated. However, in order to synthesize samples for proof of concept, the cap layer was poured slowly from the edge, and the areas of material used for later analysis were taken from undisturbed regions near the center of the sample to maximize uniformity of the layers in the area of study.

The benefits of this method are that the phosphor is incorporated during the aerogel synthesis and there is good aerogel layer bonding as seen in Figure 10c.

Method 2. A sol-gel solution was poured into a silicone mold like in Method 1. However, instead of a phosphor-methanol mixture, a 50% La_2O_2S:Eu phosphor-doped PDMS thin film synthesized in the manner described in Section 3.1.3 was applied to the surface of the aerogel. A cap layer of sol-gel solution was poured over the thin film encapsulating it completely. The remaining synthesis steps were followed, including the extra flushes as described for Method 1.

The solvent flushing posed complications in this method also. Even with additional flushes in the solvent exchange, the PDMS inhibited full solvent exchange. During out-gassing in the CPD, the aerogel samples containing the interfacial film fractured, and in some areas collapsed. This protocol of incorporating phosphor into aerogel synthesis was unsuccessful. This method was first attempted using crosslinked aerogel shown in Figure 10f. The reduction in clarity seen in the image is a result of incomplete solvent exchange. The next synthesis round was done using non-crosslinked aerogel. The hypothesis was that excluding the Desmadur from the synthesis as in the non-crosslinked aerogel would increase the availability for the solvent exchange and

prevent fracture and collapse of the aerogel. This was not the case, however. The aerogel layers in this sample split apart and fractured, exposing the thin film as can be seen in Figure 10e.

Method 3. A segment cut from a fully synthesized crosslinked aerogel disk was placed on a Chemat Scientific spin coater. 1 mL of uncured 50% phosphor-doped PDMS slurry was pipetted directly onto the surface of the aerogel. It was spun at 1000 rpm for 18 s, the same conditions used in Section 3.1.3 for the doped thin films. A matching cap piece of aerogel was placed on top. The PDMS in the layered structure was allowed to cure at room temperature for 3 days, gluing the aerogel layers together.

This method was an effective means of including phosphor as a discrete layer in aerogel as shown by Figure 10g. However, there were challenges with getting full layer bonding due to small imperfections in the aerogel surface which occurred post drying stage. This can be seen in Figure 10h. This method of creating a layered structure is viable but less sophisticated than incorporating the phosphor during synthesis.
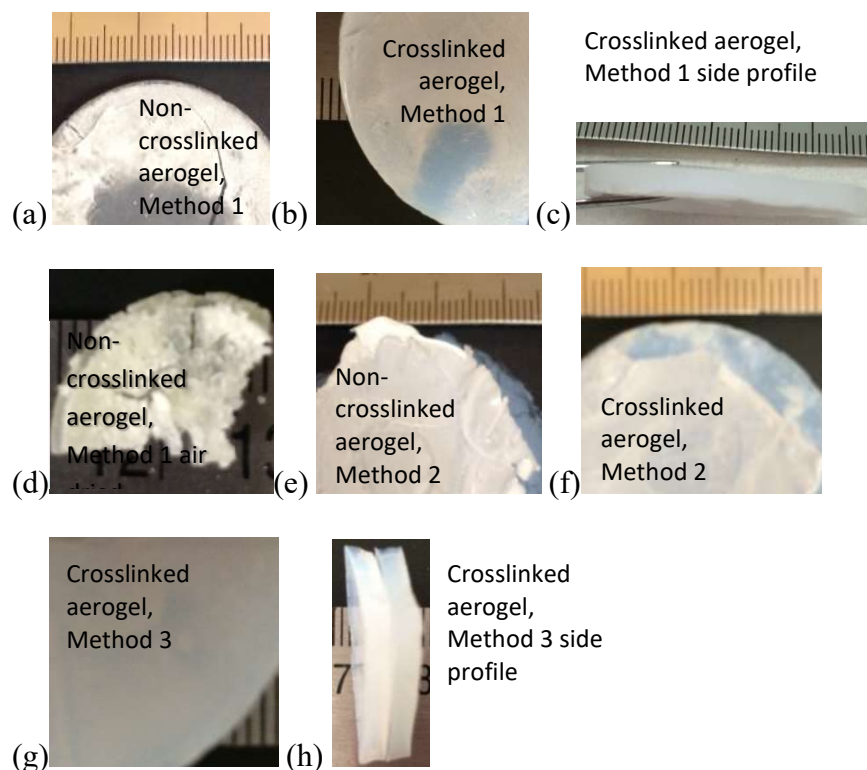
Figure 10: Optical images of crosslinked and non-crosslinked samples synthesized via Methods 1, 2 and 3. It was determined that Method 1 was the most successful for incorporating phosphor into the aerogel synthesis due to the lack of fracture or collapse and good adhesion between layers.

3.1.5 PDMS-Phosphor Composites

Phosphor-layered PDMS structures were constructed to mirror the phosphor-layered aerogel structure. Sylgard-184 base and crosslinker was mixed 10:1, according to manufacturer instructions. The mixture was poured into an aluminum boat to reach a desired 2 mm thickness. It was outgassed and then cured at 100°C for 1 hr. The PDMS was left in the mold for the next 2 layers. For the phosphor layer, $La_2O_2S:Eu$ powder was added to 50% weight doping to the uncured PDMS. The slurry was well mixed and

outgassed. A small amount was poured onto the surface of the cured PDMS in the mold.

It was mounted to a spin coater and spun at the conditions described in Section 3.1.3. The

PDMS was then placed in the oven again for 1 hr at 100°C to cure. After curing, a final 2

mm layer of neat PDMS was added to the top in the same manner as the first layer. After

curing, the layered structure was removed from the boat. A schematic of the structure

synthesized with PDMS and phosphor is below in Figure 11.

Figure 11: Schematic diagram of PDMS sample made with a layer of phosphor-doped
PDMS mirroring Method 2 of the aerogel synthesis configurations used in parallel to the
aerogel sample synthesized and used for experimentation via Method 1.

3.2 Sample Characterization

Several characterization tools were used to understand the properties of the

prepared samples and new non-crosslinked aerogel recipe. These methods are described

below;

3.2.1 Thermal Conductivity

Measuring thermal conductivity of powders: Thermal conductivity measurements

were taken with a Hot Disk TPS 1500 by Therm Test using the powder cell configuration

shown in Figure 12a. The thermal conductivities of $Mg_3F_2GeO_4{:}Mn$ and $La_2O_2S{:}Eu$

phosphor in powder form were measured. In each case, phosphor powder was packed

into a hollow cylinder of diameter 2.5 cm and height of 6 mm. A two-sided Kapton

sensor with a radius of 6.403 mm was placed on the surface of the powder. Another hollow cylinder of 2.5 cm diameter was stacked on the sensor, and 6 mm height of powder was filled in on top of the sensor. The powder was repeatedly packed down with a solid cylinder of 2.5 cm diameter to eliminate air gaps. The total volume filled was 6.38 cm^3. For La$_2$O$_2$S:Eu, the required mass of powder was 15.52 g. For Mg$_3$F$_2$GeO$_4$:Mn, 6.29 g was needed. 10 measurements were taken of each phosphor and averaged to determine the thermal conductivity. Measurements were also taken with a larger volume of powder to ensure any trapped air did not affect the results. For this set of measurements, the total volume used was 12.76 cm^3. The volume configurations are depicted in Figure 12b.

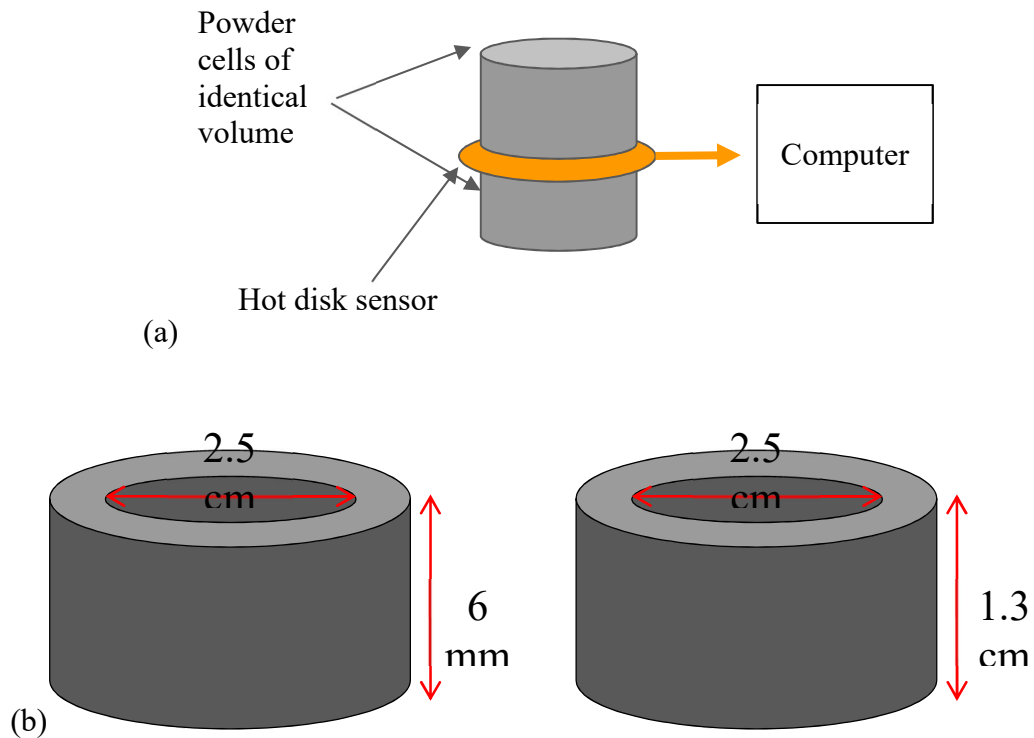Figure 12: Highlights of thermal conductivity set up as described in Section 3.2.1: (a) Hot disk sensor configuration for phosphor powder thermal conductivity measurements where the grey cylinders are hollow for holding powder. (b) Sizes of powder cells used in measurement configuration where 2 volumes were used to ensure the thermal conductivity measurements were volume independent due to unavoidable trapped air.

Measuring thermal conductivity of monoliths: To measure the thermal conductivity of non-crosslinked aerogels, cylindrical samples with a diameter of 1.25 cm and height of approximately 0.5 cm were stacked on either side of a two-sided Kapton sensor with a radius of 3.189 mm. This size sample was used to ensure the material mimicked an infinite size relative to the sensor diameter which is required to obtain accurate results using the TPS method. 5 measurements were collected, and the thermal conductivity values averaged to determine the average thermal conductivity.

3.2.2 UV-Visible Spectroscopy

An Evolution 220 UV-Vis spectrophotometer with an integrating sphere attachment was used to measure absorbance, transmission, and reflection of the crosslinked aerogel, non-crosslinked aerogel, and PDMS samples. The transmission measurement was of direct transmission with an incident angle of $0°$. When necessary, a quartz slide was used to mount samples due to its optical transparency in the UV-Vis range. When using the integrating sphere, Spectralon was used as the background calibration; the quartz slide was not needed to mount the samples when using the integrating sphere. The reflection measurement with the integrating sphere was of diffuse reflectance. Total transmission was not measured with the integrating sphere because the equipment configuration was not suitable for the samples made. With the direct transmission and specular reflectance measured, the remaining incident light is either absorbed or scattered as specular transmission and together is considered attenuance. Measurements were taken on each aerogel and PDMS sample at varying thicknesses to characterize the optical properties of the materials and identify optimal material properties. Due to the optical applications of the materials used in luminescent studies,

understanding the ability for the light source to access the phosphor embedded in the material was key to the luminescent experiments.

3.2.3 Porosimetry

A NOVAtouch LX2 from Quantachrome Instruments was used to perform nitrogen porosimetry and measure the surface area and pore size of non-crosslinked aerogels synthesized for this study. Aerogel in powder form was placed in a glass tube and heated at 90°C for 10 hrs to thoroughly dry the sample. The sample was chilled to cryogenic temperature. Data collected from this characterization method is discussed in the next chapter.

3.3 Methods for Imparting Controlled Structural Damage

Initially, a Mark-10 ESM303 tensile tester was used in an attempt to apply controlled damage to both materials, PDMS and aerogels. The tensile tester was used because it can administer consistent amounts of force on each sample. However, the non-crosslinked aerogel was so fragile that the level of control needed to impart any amount of damage short of full breakage could not be obtained by the available equipment. Also, the PDMS was so elastic that it recovered and demonstrated self-healing behavior. Therefore, a different method was needed for a pilot study to allow for consistency and control.

A razor blade was used to carve a wedge 1 mm wide and approximately 0.5 mm deep into a piece of neat PDMS of 2 mm thickness. A CRL diamond-tipped scribing tool was used to carve a wedge 1 mm wide and 0.1 mm deep into a piece of clean cross-linked

aerogel of 2 mm thickness. Cross-linked aerogel was used due to the fragility of non-crosslinked aerogel in this approach. The wedge cut in each material is depicted by the schematic in Figure 13.
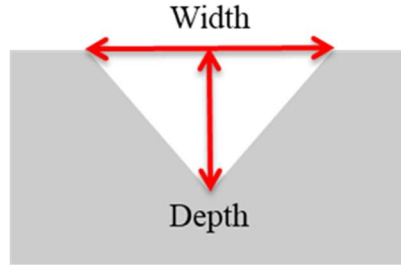
Figure 13: Schematic diagram of damage imparted on crosslinked aerogel and PDMS. A wedge of width 1 mm was cut 0.5 mm deep into PDMS and 0.1 mm deep into crosslinked aerogel.

3.4 Experimental Set-Up for Luminescence Measurements

An MK 1000 INSTEC heating-cooling stage equipped with a liquid nitrogen cooling mechanism was used to perform luminescence measurements at different temperatures. The stage, detector, and source were contained in a humidity controlled ETS environmental chamber, fully sealed. The humidity control system was capable of reducing the humidity level from 78 % to 5 % and was able to retain at this level for the duration of the measurement. To reduce interference from ambient light, the environmental chamber was wrapped in an opaque film to block ambient light. A 405 nm laser diode was used as the excitation source for both $La_2O_2S:Eu$ and $Mg_3F_2GeO_4:Mn$. A TTL pulse from BNC model 575 Pulse Delay Generator was used to control the laser duration and rate. The phosphor emission was detected by a photomultiplier tube (PMT) with a filter that selects the emission wavelength for the excited band. The optical signal

detected was converted to an electronic signal by the PMT and shown on a 100 MHz

Tektronics TDS 2012-C oscilloscope. The heating-cooling stage had a precision of

0.001°C. A schematic diagram of the set-up is shown in Figure 14.
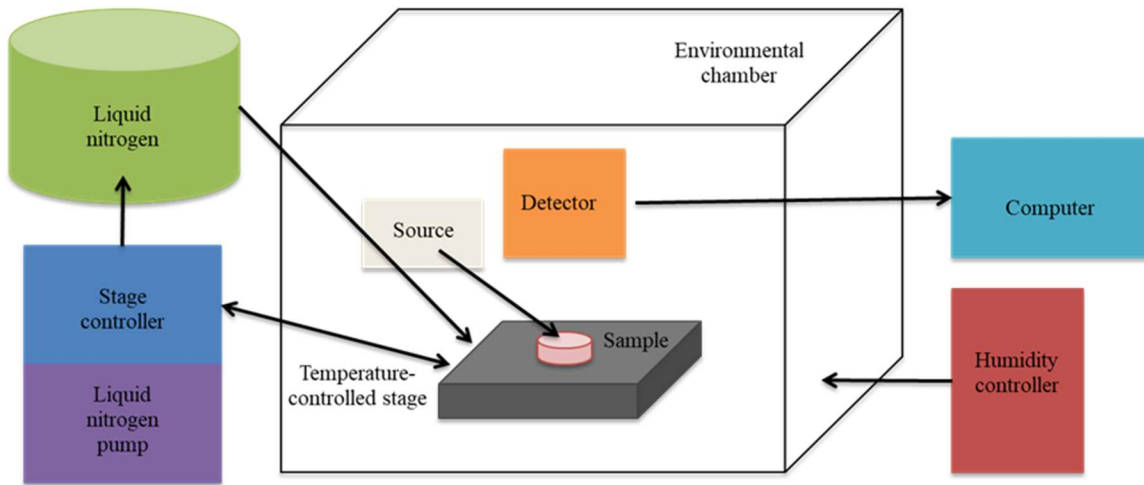
Figure 14: Schematic diagram of experimental setup used for luminescent data collection showing the major components of equipment in block diagram form, where the temperature-controlled stage, excitation source, and detector were contained in a humidity-controlled environmental chamber.

3.4.1 Luminescence Analysis of Damaged Samples

Two configurations of samples with varying degrees of structural damage were

analyzed with the luminescence set up describe in the previous section to determine the

feasibility of using thermographic phosphors for damage detection using aerogel and

PDMS.

Configuration 1: An extreme case of structural damage, complete breakage

through the material, was simulated using two cut segments of 2 mm thick non-

crosslinked aerogel. The two segments of aerogel were placed next to each other with a

50% La$_2$O$_2$S:Eu-doped PDMS thin film, synthesized as described by Section 3.1.3,

placed over the segments ensuring the film adhered to the surface of the material. The

configuration was placed on the temperature-controlled stage as shown by the schematic

diagram in Figure 15a. Measurements were taken on the thin film over the surface of the

aerogel and on the thin film over the gap between the segments of aerogel at several

temperatures ranging from -60°C to 200°C. At each temperature, measurements were

collected with varying separations between the segments of material: 5 mm, 2 mm, 1

mm, and 0 mm. The experiment was also performed with 5 mm and 10 mm non-

crosslinked aerogel, as well as 2 mm and 10 mm crosslinked aerogel. Table 2 outlines the

combinations of material type, material thickness, and temperatures used.

For the sake of consistency, each sample was allowed to sit on the temperature-

controlled stage for 5 mins before measurements were collected.

Table 2: Stage temperatures, material types, and material thicknesses used for experimentation with samples constructed in accordance with Configuration 1.

Stage Temperatures and Samples Used for Luminescence Measurements					
	PDMS		Non-crosslinked Aerogel		
Temp (°C)	2 mm	10 mm	2 mm	5 mm	10 mm
-60	X	X	X		X
-40	X	X	X		X
25	X	X	X		X
70	X	X	X	X	X
100	X	X	X	X	X
150	X	X	X	X	X
200	X	X	X	X	X

Configuration 2: The damage protocol described in Section 3.3 was followed for a cut segment of 2 mm thick crosslinked aerogel where a wedge was carved into the material without cutting all the way through the material. A 50% La_2O_2S:Eu-doped PDMS thin film was placed on the surface of the sample, ensuring adhesion, like Configuration 1. Measurements were taken over the damaged portion and on the untouched surface as shown in Figure 15b. The same temperatures between -60°C to 200°C were used for Configuration 2 as were used for Configuration 1. Again, each sample was left on the stage for 5 mins, but the same error described for Configuration 1 was also built into this data set also. This experiment was repeated for a 2 mm thick PDMS sample also with the same damage protocol described in Section 3.3.
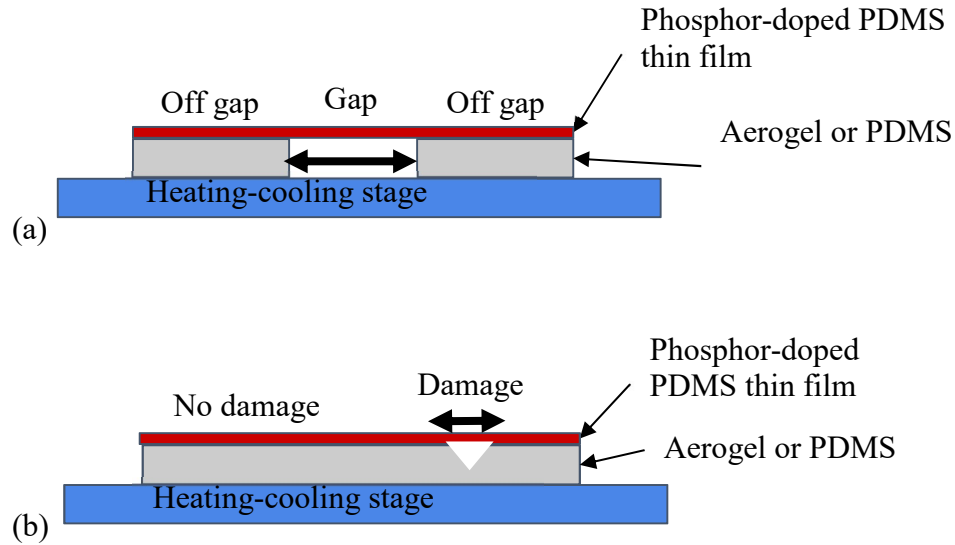
Figure 15: (a) Schematic of Configuration 1 for luminescence measurements of where the material is fully separated to represent catastrophic or extreme material failure, used to identify feasibility of concept. (b) Schematic of Configuration 2 where a wedge is cut out of the material, not completely dividing it into two, to represent a material crack or fracture, used to predict whether the methodology had high enough resolution to warrant further study.

3.5 Decay Time and Temperature Calculations

Decay times and temperatures were extracted from the raw luminescence data as described by published methods (37). Because, despite best efforts, there was background light, the average intensity of data points from background light was subtracted from the remaining data as a background subtraction. The signal was scaled by the maximum signal to normalize the data. The semi-log of signal voltage vs. time was plotted to extract the slope. The negative inverse of the slope was calculated to find decay time. To calculate temperature from decay time, a calibration curve unique to the phosphor powder and excitation band was used.

Chapter 4

Results and Discussion: Sample Properties and Characterization

4.1 Gravimetric Analysis of Aerogel Samples

The densities of all aerogel samples prepared for this study were calculated and have been summarized in Table 3. Crosslinked aerogel samples of thicknesses 5 and 10 mm were not synthesized. It was hypothesized that crosslinked aerogels of such thicknesses would cause a significant amount of light scattering and attenuation and as a result, would allow very limited optical access to embedded phosphor layers. For non-crosslinked aerogels average densities vary from 0.11 g/cm^3 to 0.36 g/cm^3 and for crosslinked aerogels average 0.51 g/cm^3. The calculated densities for both crosslinked and non-crosslinked aerogels show some variation from batch to batch, and to a degree some dependency on the geometry of the final sample. Crosslinked aerogels are expected to have a greater density when compared to non-crosslinked aerogels. The amount of surface area available for solvent exchange does affect outgassing efficiency and as a result the final density of the dried aerogel. Both aerogel types have densities within the range of published values for these aerogel types (91).

Table 3: Densities of crosslinked and non-crosslinked aerogel samples with varying thickness, where the non-crosslinked aerogels of all thicknesses were less than the density of crosslinked aerogel at 2 mm. Crosslinked aerogels were not synthesized at 5 mm and 10 mm because they were not necessary for this work.

Aerogel Densities of Samples with Varying Thickness			
	Density (g/cm^3) by Thickness		
Aerogel Type	2 mm	5 mm	10 mm
Non-crosslinked	0.21 ± 0.01	0.11 ± 0.01	0.36 ± 0.01
Crosslinked	0.51 ± 0.01	N/A	N/A

4.2 Thermal Conductivity of Phosphor Powders and Non-crosslinked Aerogel

The thermal conductivity of both types of phosphor used in this study was measured at room temperature, while in powder form. La_2O_2S:Eu and $Mg_3F_2GeO_4$:Mn were added to insulating materials, aerogels and PDMS, to create composites. It was necessary to learn what the thermal conductivity contribution was from these compounds. These measurements have been summarized in Table 4 and averaged over five separate measurements. Neither La_2O_2S:Eu nor $Mg_3F_2GeO_4$:Mn are expected to contribute significantly to the thermal conductivity of the composite material and as a result are not expected to alter the insulative properties of either material, aerogel or PDMS noticeably. The thermal conductivity of La_2O_2S:Eu was approximately 0.02 W/mK less than $Mg_3F_2GeO_4$:Mn.

For comparison, the thermal conductivity of Sylgard 184 and aerogels were measured and are provided in Table 5. Non-crosslinked aerogels have a K value in the range of 0.06 w/mK. The K value measured for the phosphor powders is approximately a

46

factor of two greater than the values typically measured for non-crosslinked aerogels. Ideally, the phosphor layer would be confined to a monolayer in the aerogel monolith. In this work we were not able to measure the K value for the composite material. Our system can only measure homogeneous samples. To a first approximation we have calculated the K value for the composite material using the sum of the conductive resistance for each layer, as described in Section 2.1, as K = 0.0595 W/mK. This is within 0.005 W/mK of the average thermal conductivity of non-crosslinked aerogel. This calculation assumed a composite according to Method 1, as described in Section 3.1.4, with 2 mm thick aerogel layers, a 0.1 mm thick phosphor layer, and surface area of 2 cm^2.

The thermal conductivity of Sylgard 184 reported here is much closer to that of the phosphor powders than non-crosslinked aerogel. Therefore, embedding the PDMS with phosphor powder would not significantly impact the thermal conductivity of the material. The thermal conductivity of non-crosslinked aerogel has a thermal conductivity an order of magnitude less than the phosphor powders. This indicates that embedding the phosphor within the aerogel material could alter the heat conduction behavior of the non-crosslinked aerogel.

Table 4: Thermal conductivity values and corresponding masses used for phosphor powders

Thermal Conductivities and Masses of Phosphor Powder Used for Varying Volumes and Phosphor Types				
	$V_1 = 10.8$ cm^3		$V_2 = 22.6$ cm^3	
Powder Type	k (W/mK)	Mass (g)	k (W/mK)	Mass (g)
$La_2O_2S:Eu$	0.111 ± 0.0001	15.52 ± 0.01	0.110 ± 0.0007	61.76 ± 0.01
$Mg_3F_2GeO_4:Mn$	0.129 ± 0.0001	6.29 ± 0.01	0.127 ± 0.0006	29.40 ± 0.01

Table 5: Thermal conductivity values for solid samples, non-crosslinked aerogel and Sylgard 184 (20).

Thermal Conductives of Non-crosslinked Aerogel and Sylgard 184	
Material	k (W/mK)
Non-crosslinked aerogel	0.06 ± 0.0002
Sylgard 184	0.17

4.3 UV-Visible Spectroscopy

Samples of non-crosslinked and crosslinked aerogels as well as Sylgard 184 at varying thicknesses were analyzed by UV-Vis spectroscopy as described by Section 3.2.2 and discussed in detail below.

Reflectance: The reflectance signal for 2 mm thick non-crosslinked aerogel sample (Figure 17a) is less than 10% for incident wavelength between 200 nm and 800 nm. For the samples of 5 mm thickness, the reflectance is less than 10% below approximately 350 nm. However, the signal peaks to approximately 20% around 350 nm with a steady decrease in reflectance from that point to 800 nm where the reflectance drops to approximately 5%. This trend in reflectance scattering is due to the Rayleigh theory of scattering as described in Section 2.8.3. The incident wavelength is 3 to 4 orders of magnitude greater than the pore size of the aerogel, so the reflectance intensity is proportional to λ^{-4}. As the incident wavelength increases, the amount of reflectance scattering decreases. Crosslinked aerogel, as shown in Figure 17b, follows a similar trend. The reflectance peaks just below 400 nm and decreases with increasing wavelength. The reflectance is greater for the 4 mm thick crosslinked aerogel than the 2 mm. The addition of Desmodur may further decrease the pore size and increase the surface roughness, both of which can lead to higher reflectance values. The reflectance

measurements of all 4 aerogel samples are shown together in Figure 17d. Increasing the aerogel thickness increases the reflectance, as previously mentioned. But also, the thinnest crosslinked aerogel of 2 mm has a higher reflectance intensity than the thickest non-crosslinked sample of 5 mm thickness. The difference in intensity between the crosslinked aerogel samples at the peak is approximately 15%. For non-crosslinked aerogel, the difference in peak is between 10% and 15%. However, the change in reflectance between the 2 mm crosslinked aerogel and 5 mm non-crosslinked aerogel is approximately 20%. This indicates that the presence of crosslinker affects reflectance more than the thickness of the sample. The reflectance of PDMS of 2 mm and 10 mm thicknesses is shown in Figure 17c. Reflectance across all wavelengths from 200 nm to 800 nm is approximately 10% and constant.

Absorbance: According to the Beer-Lambert law, absorbance is proportional to material thickness. The plotted attenuance for non-crosslinked aerogel in Figure 17a also contains diffuse transmission as well as the absorbance. The attenuance is greater for all wavelengths below 200 nm up to 800 nm, the range that was measured. The absorption is greater for the 5 mm thick non-crosslinked aerogel than the 2 mm sample. However, the attenuance is not proportional between the two samples. The difference in attenuance is greater for the incident wavelength around 450 nm. As the wavelength increases, the difference in attenuance decreases. The absorbance for crosslinked aerogel in the UV range, as shown in Figure 17b, is inversely related to reflectance due to a negligible transmittance. PDMS absorbs strongly in the UV range. Both thicknesses are almost saturated from 200 nm to 300 nm, averaging around 90% attenuance. Considering the

low scattering that PDMS exhibits, it can be surmised that a negligible portion of the attenuance is due to scattering.

Transmittance: The transmittance of non-crosslinked aerogel as shown in Figure 17a increases from 400 nm to 800 nm as predicted by the Raleigh scattering theory as described in Section 2.8.3. For aerogel, because reflectance decreases with increasing wavelength in this range and absorbance is less dominant, the transmittance increases with increasing wavelength. The increase in the 5 mm sample is more rapid than the 2 mm sample. This is a result of the thicker sample having a higher absorbance. For crosslinked aerogel, as shown in Figure 17b, the transmittance is approximately 0% between 200 nm and 400 nm. For the 2 mm thick sample, transmission increases from 400 nm to 800 nm in the same manner as the 5 mm non-crosslinked aerogel. For the 4 mm crosslinked sample, the transmission was approximately 0% until 500 nm instead of 400 nm. The differences in transmission between the two crosslinked aerogel samples is approximately the same; however, the transmission of the 2 mm sample increases faster than the 4 mm sample, similar to the non-crosslinked aerogel. Figures 16a and 16b show photographs of non-crosslinked and crosslinked aerogel, where the difference in transparency is apparent to the naked eye. Figure 17e shows the transmission spectra for all 4 aerogel samples. Unlike the reflectance spectra, the crosslinked and non-crosslinked aerogel alternate transmission intensity, where the 2 mm samples have higher intensities than the thicker samples. This indicates that for aerogel, thickness impacts transmittance more than the inclusion of crosslinker. The non-crosslinked aerogel of 2 mm thickness is the only sample which transmits in the UV range to any degree.

The transmittance of PDMS is shown in Figure 17c. There is approximately 0% transmission in the UV range. The transmission of 2 mm thick PDMS above 400 nm is above 95%, approximately. However, there is a drop in the transmission curve for the 10 mm PDMS. This is an unexpected result as PDMS has little scatter or absorption in the visible light range. Errors in measurement could be due to micrometer-sized trapped air bubbles not visible to the naked eye within the material resulting from incomplete outgassing.

For accessing phosphor embedded in the aerogel, understanding the optical properties of the material provides indication of the optimum sample parameters for gaining optical access to embedded phosphor. If the incident light source is impeded from reaching the phosphor due to scatter or absorption or if the wavelength of characteristic emission is absorbed before reaching the surface of the material, the material is not useful for the desired application as a phosphor encapsulant. Based on the spectra, each material presents promising properties as well as potential drawbacks for optical applications involving embedded phosphor. Further experiments were performed to ensure the embedded phosphor was both accessible in the material and the luminescent emission was detectable.
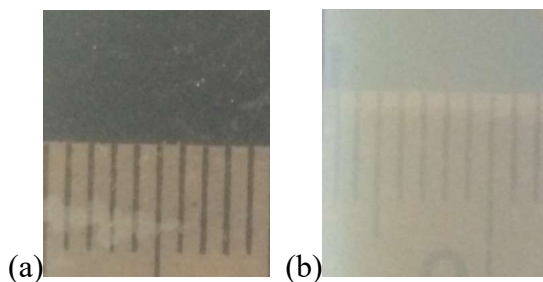
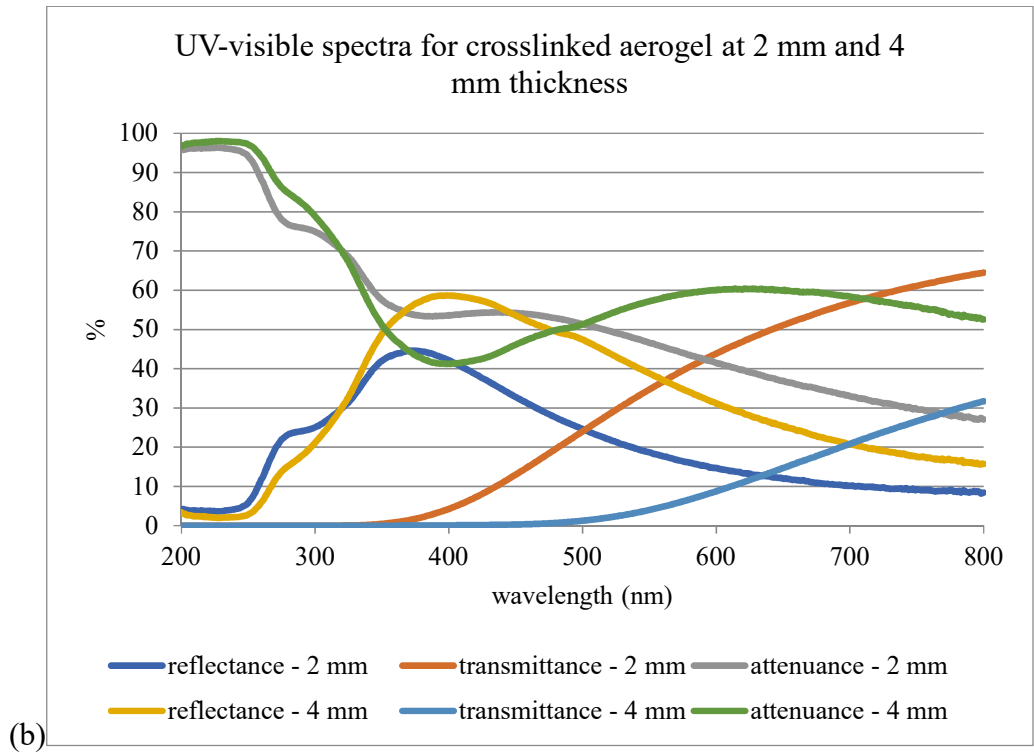Figure 16: Optical images of 2 mm thick (a) non-crosslinked aerogel and (b) crosslinked aerogel showing changes to degree of transparency/opacity.

UV-visible spectra for non-crosslinked aerogel at 2 mm and 5 mm thickness

(a)

UV-visible spectra for crosslinked aerogel at 2 mm and 4 mm thickness

(b)

UV-sisible spectra for PDMS at 2 mm and 10 mm thickness

(c)

reflectance - 2 mm
transmittance - 2 mm
attenuance - 2 mm
reflectance - 10 mm
transmittance - 10 mm
attenuance - 10 mm

Reflectance of crosslinked and non-crosslinked silica aerogel

(d)

crosslinked aerogel 2 mm
crosslinked aerogel 4 mm
noncrosslinked aerogel 2 mm
noncrosslinked aerogel 5 mm

Transmittance of crosslinked and non-crosslinked silica aerogel

Legend: crosslinked aerogel 2 mm — crosslinked aerogel 4 mm — noncrosslinked aerogel 2 mm — noncrosslinked aerogel 5 mm

(e)

Figure 17: UV-visible spectroscopy measurements of reflectance, transmittance, and attenuance collected from samples of (a) 2 mm and 5 mm thick non-crosslinked aerogel, (b) 2 mm and 4 mm thick crosslinked aerogel, and (c) 2 mm and 10 m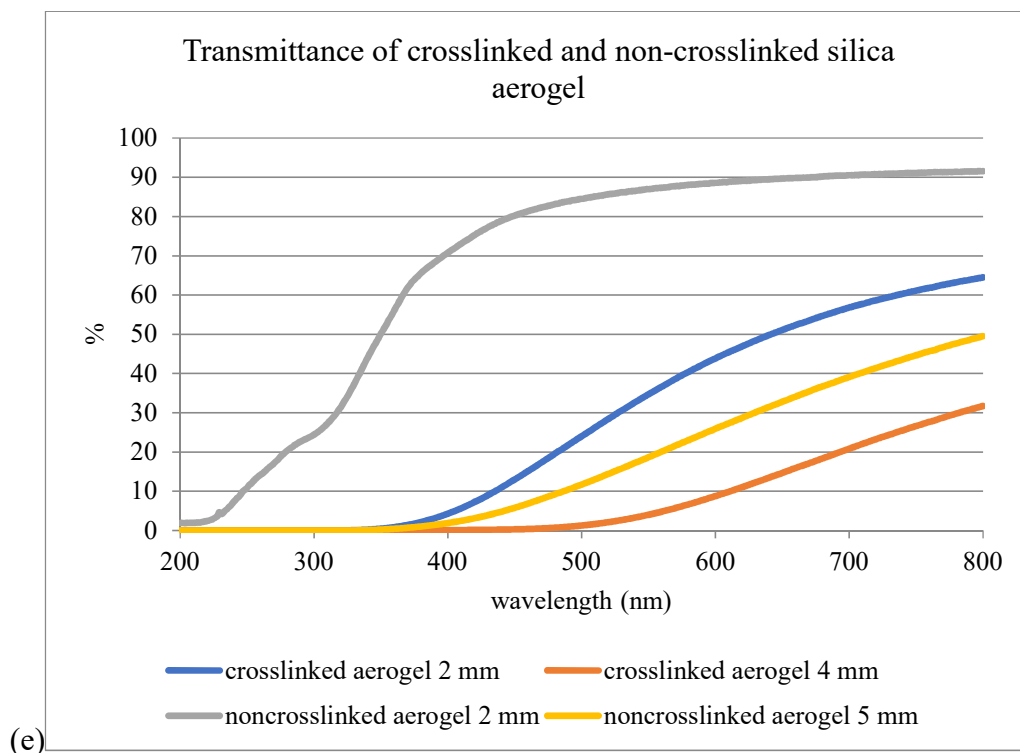m thick PDMS. Measurements of 2 mm and 5 mm thick non-crosslinked aerogel and 2 mm and 4 mm thick crosslinked aerogel: (d) reflectance and (e) transmittance.

4.4 Pore Distribution and Surface Area Analysis of Aerogels

Non-crosslinked silica aerogels were characterized via porosimetry to better understand the internal structure of the new synthesis method as described in Chapter 3. The sorption isotherm is shown in Figure 18a. The adsorption and desorption branches are almost parallel which indicates a narrow pore size distribution (1). From this isotherm, it can also be concluded that the sample is mesoporous due to the positioning of the well-defined hysteresis in the higher P/P_o range (1). Multipoint BET and BJH methods were used to characterize the surface area. The BJH method also provided pore size, pore volume, and total percentage of pore volume. The results are tabulated in Table

6. The pore size distribution is shown in Figures 18b and 18c. The pore size ranged from 0.52 nm to 5.66 nm with the largest pore fraction averaging a size of 0.5208 nm, with a total percentage of pore volume of approximately 75%. This pore distribution, size, and volume are in agreement with published values for silica aerogels (91). The pore size distribution is narrow, as shown by the percentage breakdown in Figure 18d. 99.7% of the pores are below 12.95 nm; 93.1% are less than 7.81 nm in size. 33% of the pore sizes are in the mesoporous range, between 2 and 50 nm. Reported values for silica aerogel pore diameter range from 5 nm to 100 nm with an average between 20 nm and 40 nm (92). Understanding the pore size distribution and the pore volume is significant not just for understanding the thermal conductivity behavior, but also for the optical behavior of the material.

(a)

(b)

(c)

Pareto plot of pore size distribution for non-crosslinked silica aerogel
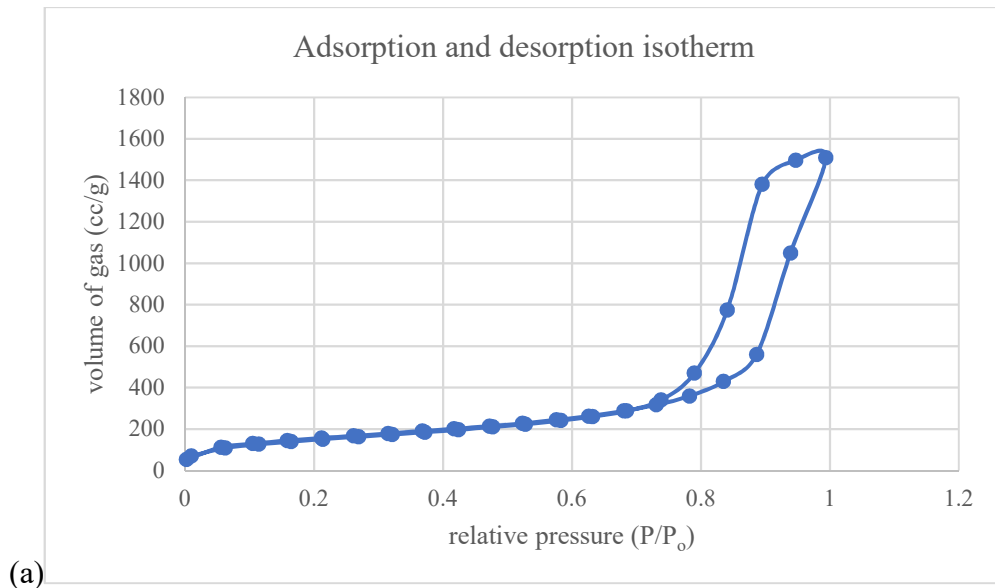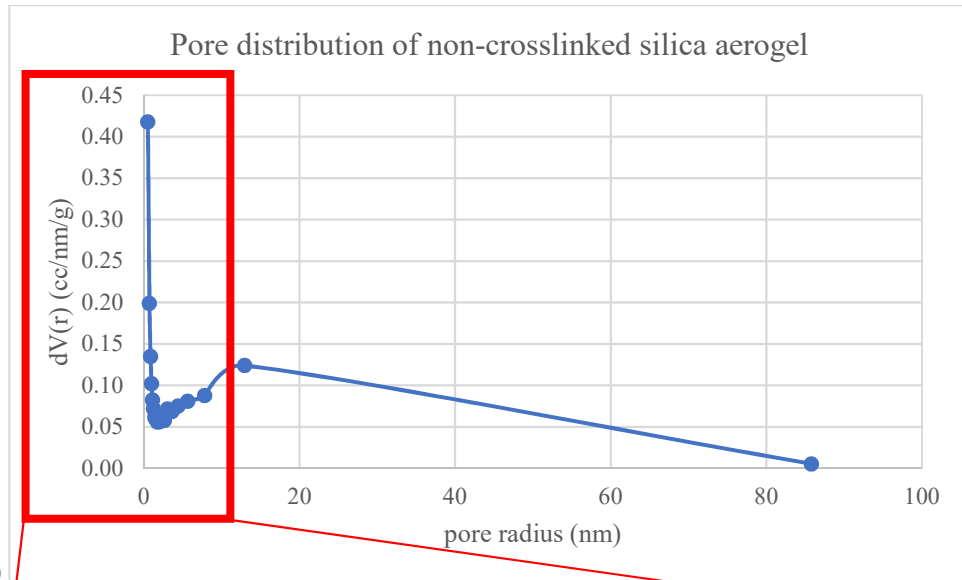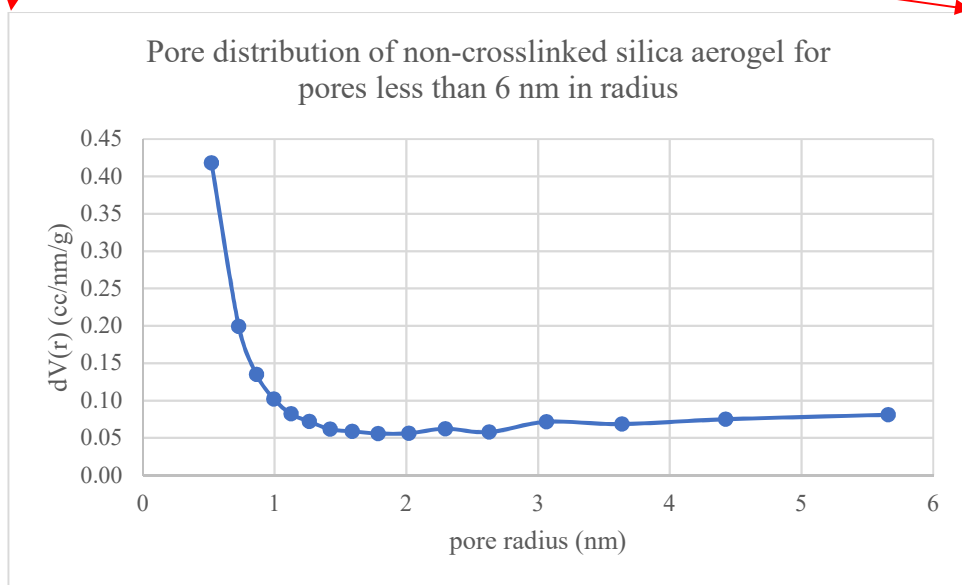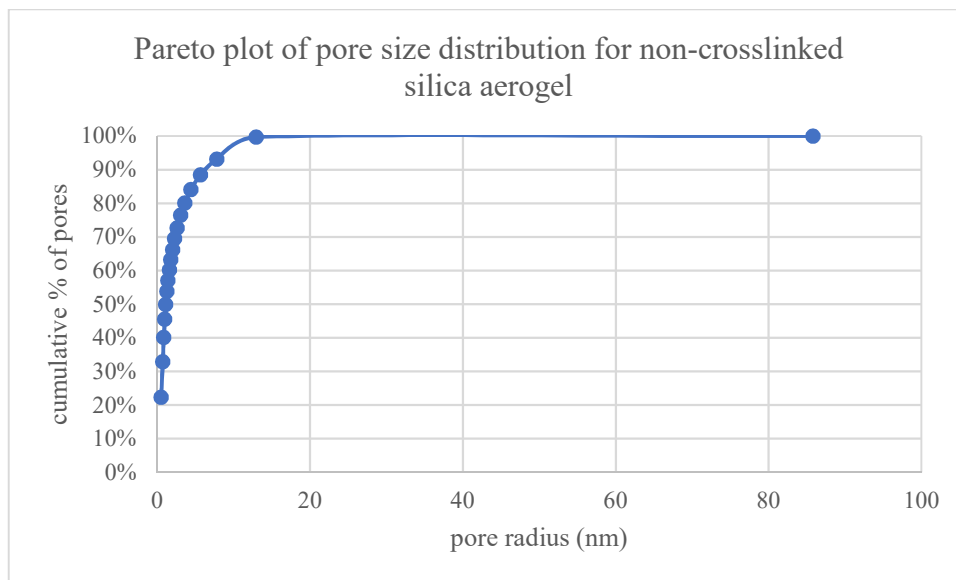
(d)

Figure 18: (a) Isotherm of non-crosslinked aerogel porosimetry. (b) Pore diameter distribution for non-crosslinked aerogel. (c) Zoom in for pore radius of less than 6 nm. (d) Pareto plot of pore size distribution for non-crosslinked silica aerogel.

Table 6: Surface area and pore information for non-crosslinked aerogel from multipoint BET and adsorption BJH methods

Porosimetry Results for Non-crosslinked Aerogel		
	BET	BJH
surface area (m^2/g)	546.55	1059.6
pore volume (cc/g)	N/A	2.47
pore radius (nm)	N/A	0.52
% pore volume	N/A	75.0%

Chapter 5

Results and Discussion: Luminescence Experiments

5.1 Assessment of Phosphor Viability Post-processing and Aerogel Synthesis

$Mg_3F_2GeO_4$:Mn powder was embedded in non-crosslinked aerogels of 2 mm thickness during synthesis, as described by Method 1 in Section 3.1.4. Tests were performed to assess the impact of the aerogel synthesis and encapsulation steps on the phosphor behavior, if any. Luminescence measurements were collected on this sample from -100°C to 80°C in steps of 2°C between -20°C and 20°C and steps of 10°C between 40°C and 80°C. The calculated decay times are reported in Figure 19 and demonstrate that (a) the embedded phosphor was accessible by excitation source and (b) produced a luminescent emission corresponding to temperature at which the composites were held. In conclusion, the phosphor powder was not damaged during the synthesis process and change in temperature resulted in an appropriate change in decay time. This result is aligned with expectations of phosphor luminescence behavior because as the phosphor gets colder, it takes longer for the electron to travel from the excited state to the ground state which results in a longer measured decay time.
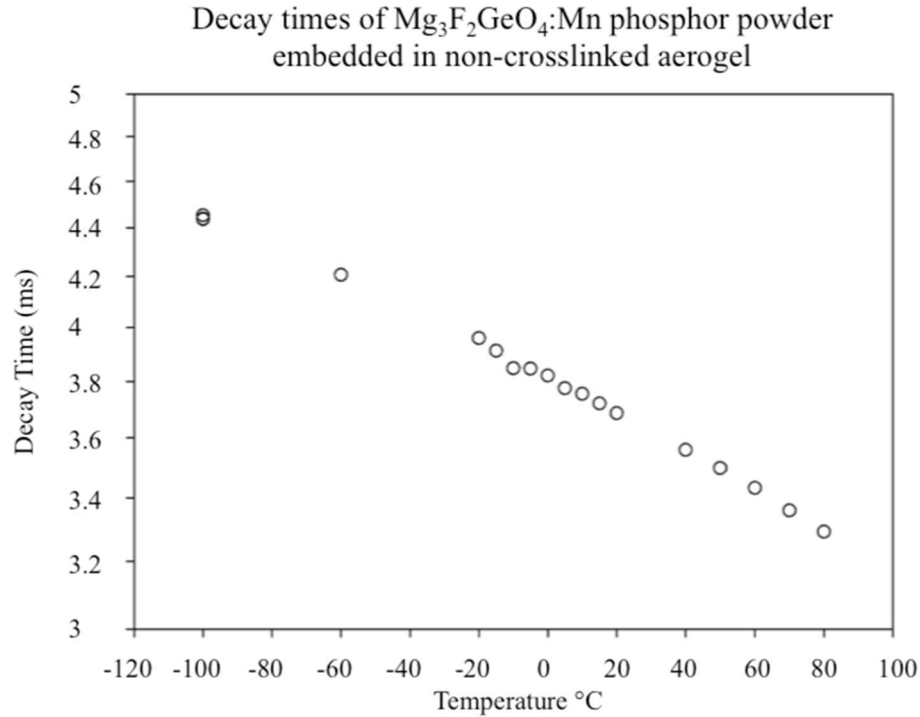
Figure 19: Decay time vs. temperature of 2 mm thick non-crosslinked aerogel containing $Mg_3F_2GeO_4$:Mn phosphor

5.2 Phosphor-Aerogel Composites for Phosphor Thermometry

It was necessary to determine (1) whether the phosphor layer embedded in the aerogel remained a discrete layer during the synthesis process and (2) if at the depth that the phosphor layer was embedded, it was still possible to excite the phosphor and detect the emitted signal. Crosslinked aerogel samples layered with La_2O_2S:Eu phosphor during the synthesis step were excited by means of a light emitting diode (LED) while held at room temperature. The optical properties of crosslinked aerogel as discussed in Section 5.1.3 had the potential to impede optical access to the phosphor layer. It was already determined that the phosphor could be accessed through non-crosslinked aerogel as described by Section 5.2.1. Therefore, an experiment was conducted to examine crosslinked aerogel. The set up for this experiment is depicted in a schematic diagram in

Figure 20a. The presence of the luminescent emission light as seen in the photograph in Figure 20c confirms that the incident light did reach the phosphor embedded in the aerogel. Otherwise, the incident light would have been scattered, reflected, and absorbed before reaching the phosphor. Adding the crosslinker reduces pore size and as a result can reduce the intensity of the signal existing the material.

It was also determined that the phosphor layer did in fact remain at a discrete layer and did not bleed into the bulk aerogel. The discreteness of the phosphor layer could be identified because on the surface of the aerogel, two distinct points of different colored light can be seen as visible in the photograph in Figure 20c. The excitation is incident at an angle. Part of the incident light is reflected when it reaches the surface of the aerogel. Part of the incident beam continues and reaches the phosphor layer, resulting in a luminescent emission originating below the surface of the aerogel. The path of the incident, reflected, and emitted signal can be traced in the schematic diagram in Figure 20a. If the phosphor was in fact dispersed throughout the material, the entire region would be illuminated, as seen in Figure 20b for example. In that case, the surface reflection of the incident light and phosphor emission would have overlapped.
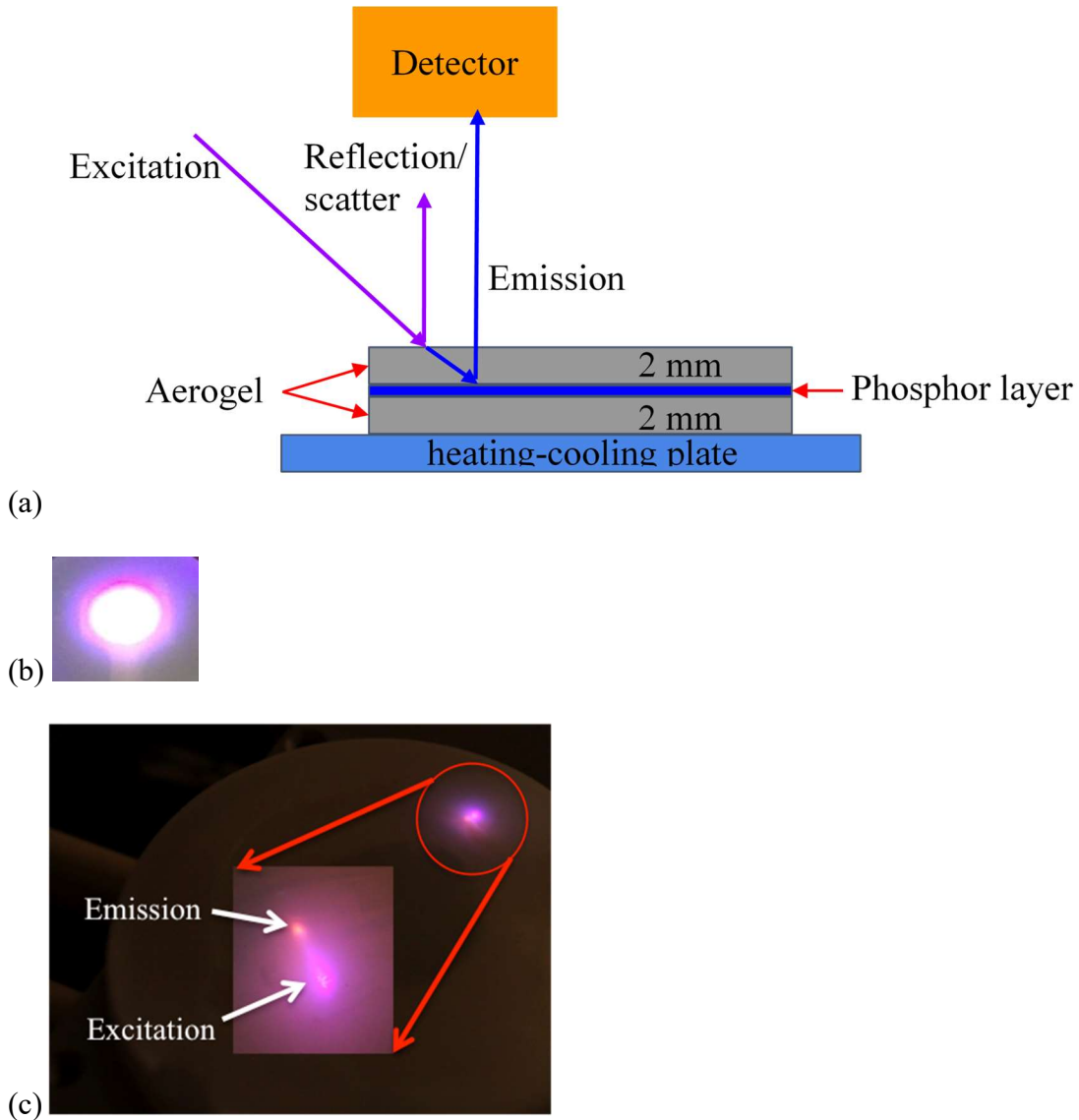
Figure 20: (a) Schematic diagram of experimental set up used to analyze crosslinked aerogel embedded with phosphor. (b) Optical image of luminescent emission from phosphor-doped PDMS where the phosphor powder is dispersed throughout the material instead of being located at a discrete layer. (c) Optical image of luminescent emission and excitation reflectance on aerogel surface where the phosphor is embedded as a layer beneath the surface of crosslinked aerogel.

5.3 Detection of Luminescent Signal as a Function of Distance

The distance-dependence of emitted signal was tested next. A 2 mm thick disk of crosslinked aerogel was placed over a 50% $Mg_3F_2GeO_4$:Mn phosphor-doped PDMS to

mimic phosphor embedded below the surface of the material. Luminescence measurements were collected and a schematic diagram of the setup is shown in Figure 21a using the sample shown in the photograph in Figure 21b. Similar setup was used for a PDMS sample. It was determined that the detector could in fact detect the emitted signal up to 1 m away for both material types. Farther distances were not measured due to technical issues. Luminescent signals through the aerogel were weaker than the signals measured from doped PDMS indicating some scatter and attenuance as a result of signal travelling through the crosslinked aerogel. Overall, a nonlinear dependency on distance was observed.

(a)

(b)

Dependence of Luminescence Detector Distance on Maximum Luminescent Output Detectable

(c)
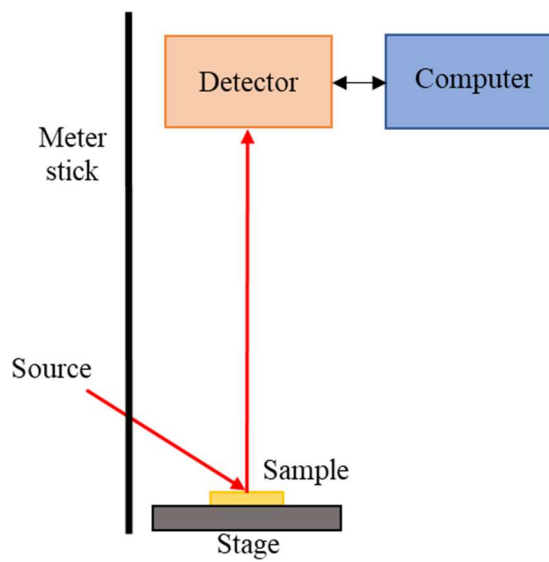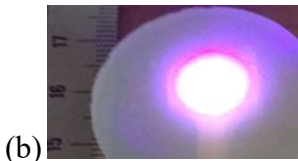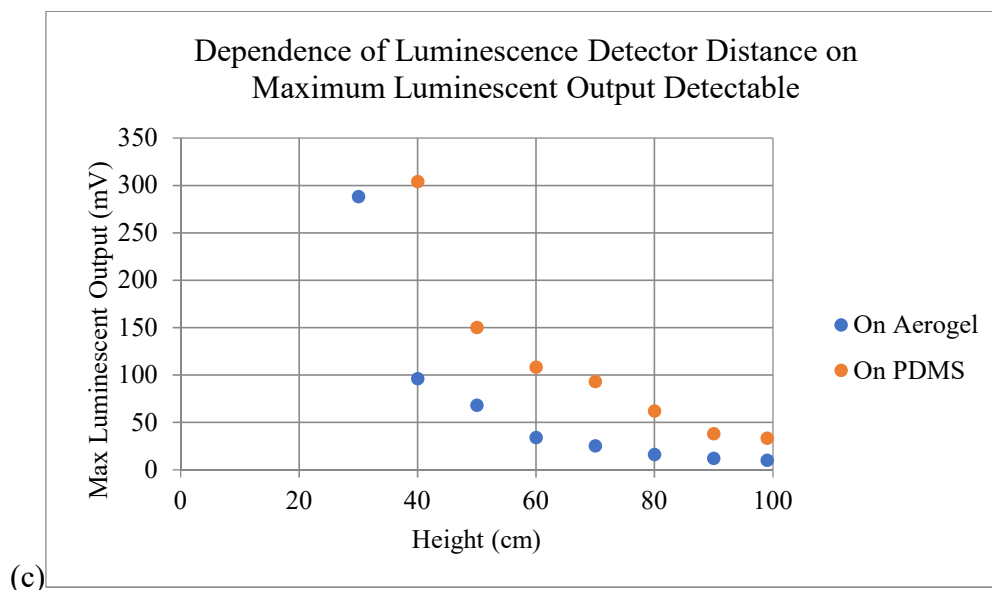
Figure 21: (a) Schematic of experiment to determine detector sensitivity to distance from sample showing the detector mounted above the stage (b) Image of crosslinked aerogel placed over 50% $Mg_3F_2GeO_4$:Mn phosphor-doped PDMS. (c) Dependence of luminescence intensity on distance for crosslinked aerogel and PDMS.

5.4 Detection of Fracture in Aerogel and PDMS by Means of Phosphor Thermometry

Configuration 1: This experiment was designed to determine whether phosphor thermometry was a viable detection method of structural damage in aerogels and PDMS or not. Measurements were taken in the same order for every sample at each temperature, initially on the gap (defect-fracture) and then on the material (non-fracture). The distance was reduced from 5 mm to 0 mm as discussed in the methods chapter. Since each luminescent signal was averaged over 30 s, the sample remained on the stage for at least 8 min to be able to collect all measurements. As a result, the surface temperature continually changed during the experiment by an unknown factor. To reduce this error,

each sample was allowed to sit on the stage for 5 mins before measurements in order to minimize experimental error.

Decay times for measurements taken on samples arranged in Configuration 1 is shown in Figure 22a. A 50% La_2O_2S:Eu-doped PDMS thin film (described in Section 3.1.3) served as the sensing element. Decay times were measured as a function of stage temperature for each sample thickness, and gap size, on two locations: (1) gap region (mimicking fracture) referred to as "on gap" and (2) the intact and untouched region of the material referred to as "off gap". These measurements were repeated for aerogels and PDMS samples in the same manner. In the case of the 2 mm and 10 mm thick PDMS samples, the decay time both on and off gap decreased as the stage temperature increased. Above room temperature, the decay times were longer for the 10 mm sample compared to the 2 mm sample, indicating a lower surface temperature for the 10 mm sample. The decay times of the 2 mm sample also increase more rapidly than the decay times of the 10 mm sample between 70°C and 200°C. Inversely, the decay times at -40°C and -60°C were longer for the 2 mm PDMS than the 10 mm PDMS suggesting that the surface of the 10 mm sample was cooler than the surface of the 2 mm sample. The decay times are disjointed at and around room temperature because the temperature dependent band in this region is different than the band of the temperatures above 100°C.

The same trend was observed for the non-crosslinked aerogel samples. The decay times decreased from 70°C to 200°C and decreased even more rapidly for the 2 mm sample than the 5 mm or 10 mm aerogel samples. It was also observed that the decay times at -40°C and -60°C were longer for the 2 mm thick aerogel sample than for the 10

mm thick aerogel. This indicates that the aerogel surface at -40°C and at -60°C was cooler for the 2 mm thick sample compared to the 10 mm sample as expected.

Temperature values were calculated from the decay times referred to in Figure 22a as described in Section 3.5 and reported in Figure 22b. Measurements taken at room temperature (stage temperature of 25°C) were excluded from analysis because at this temperature the 538 nm emission band of the chosen phosphor did not show a significant temperature dependency. For a similar reason a portion of decay times measurements at 70°C and at 100°C were also excluded due to lack of temperature dependence behavior of the 538 nm band in this temperature range. The surface temperatures of the 10 mm PDMS were less than that of the 2 mm PDMS by approximately 50°C at stage temperatures of 150°C and 200°C, as expected. The 10 mm PDMS at 70°C and 100°C had surface temperatures below the temperature dependence of the 538 nm band and could not be determined. The calculated temperature differences between off gap and on gap ($\Delta T=T_2-T_1$) was used to determine whether remote temperature sensing by means of phosphor thermometry was sensitive enough to detect fracture in PDMS and aerogels. The results are reported in Figure 22c. A positive change in temperature ($+ \Delta T$) indicates a higher surface temperature off gap compared to on gap.

For 2 mm thick PDMS at 200°C, as a function of increasing separation distance (fracture gap width), the ΔT increased above noise level. The suggests that increasing the gap width results in a significant ΔT, as detected by the thermographic phosphor. The temperature change is positive, indicating the surface temperature of the PDMS is warmer than the temperature at the fracture site. Given that the thermal conductivity of air ($K_{air}=0.04$ W/mK) is less than the thermal conductivity of PDMS ($K_{PDMS}=0.11$

W/mK (93)) at 200°C (Figure 23 (93)), the air at 200°C is a better insulator than PDMS. This means that it was expected that the PDMS would be a poorer insulator than the air at the fracture point and the surface of the PDMS would be warmer above room temperature. And this trend was measured experimentally.

For aerogel with 2 mm thickness, there did not appear to be a strong dependency of separation on gap width at any stage temperature. This is in part due to the fact that the thermal conductivity of aerogel ($K_{aerogel}$ = 0.06 W/mK) is close to the thermal conductivity of air (K_{air} = 0.04 W/mK) in this temperature range (94), and therefore heat is transferred through both mediums at approximately the same rate. This results in similar surface temperatures on and off the gap.

For the 10 mm thick PDMS sample, regardless of the gap width or stage temperature, a significant ΔT was not measured. At this thickness, the PDMS was too insulating to show a noticeable change. The same was true for the most part for the 5 mm and 10 mm thick non-crosslinked aerogels.

At 200°C, the measurements on the 10 mm thick non-crosslinked aerogel had a general increase in temperature change with increasing separation. This temperature change was negative, unlike the 2 mm thick PDMS at 200°C, indicating that the surface temperature of the aerogel was better insulating that the surface temperature of the PDMS as expected.

From this experiment, it was concluded that for both non-crosslinked aerogel and PDMS with certain parameters, a detectable change in temperature around the area of damage could be detected by the phosphor thermometry technique. The insulative

behavior of the materials chosen for this study do create challenges that should be addressed in future studies.

(a)

(b)
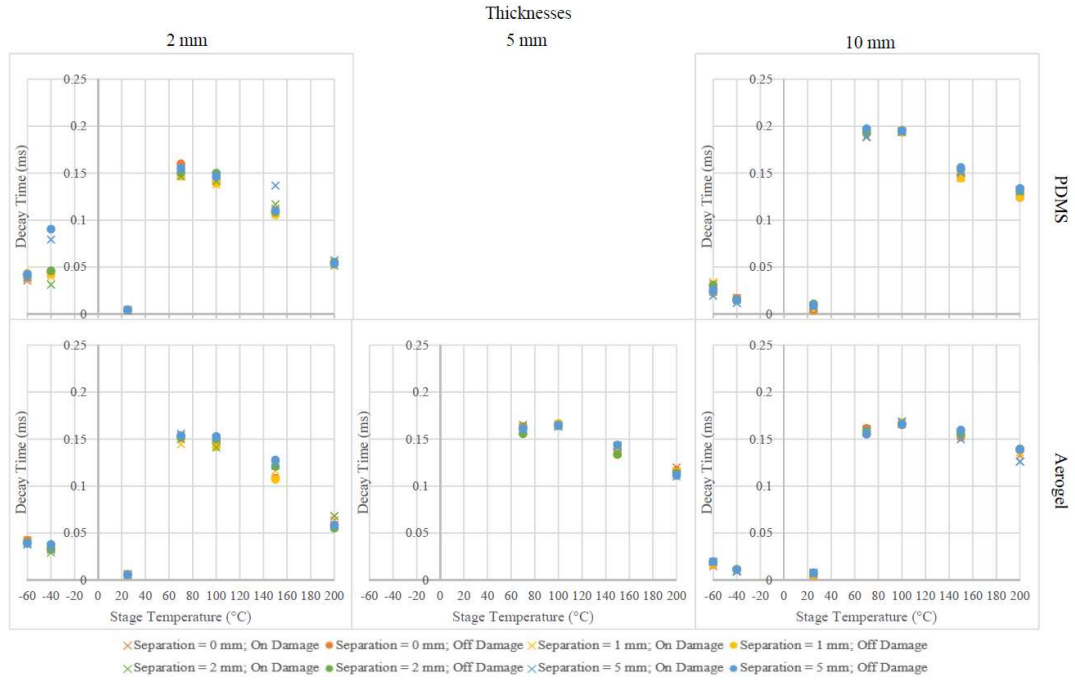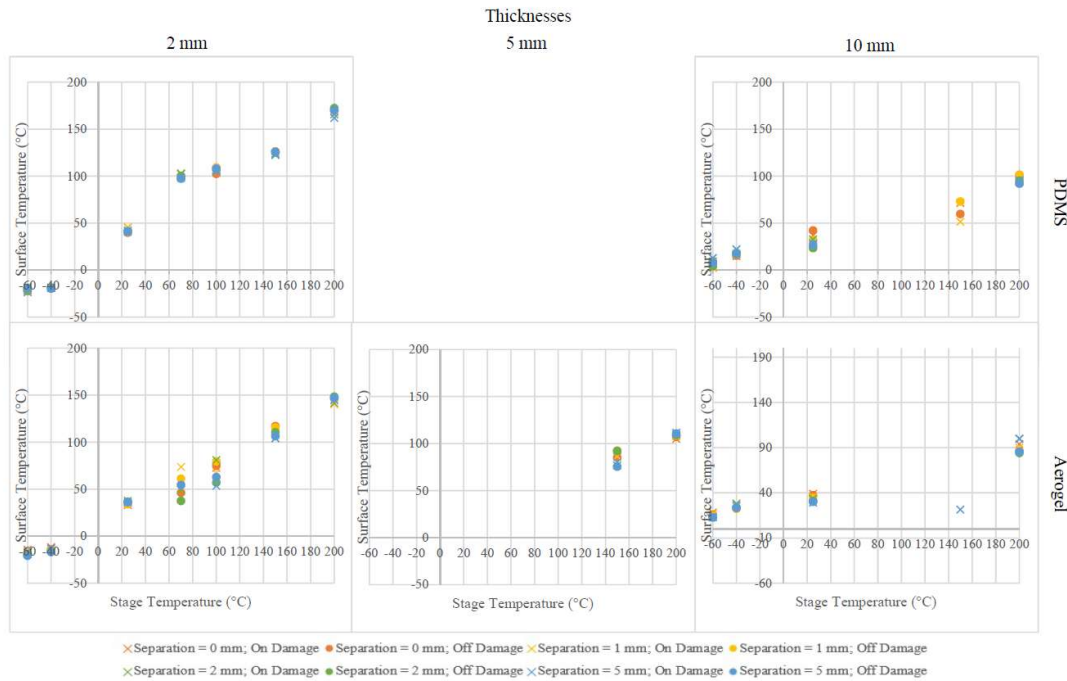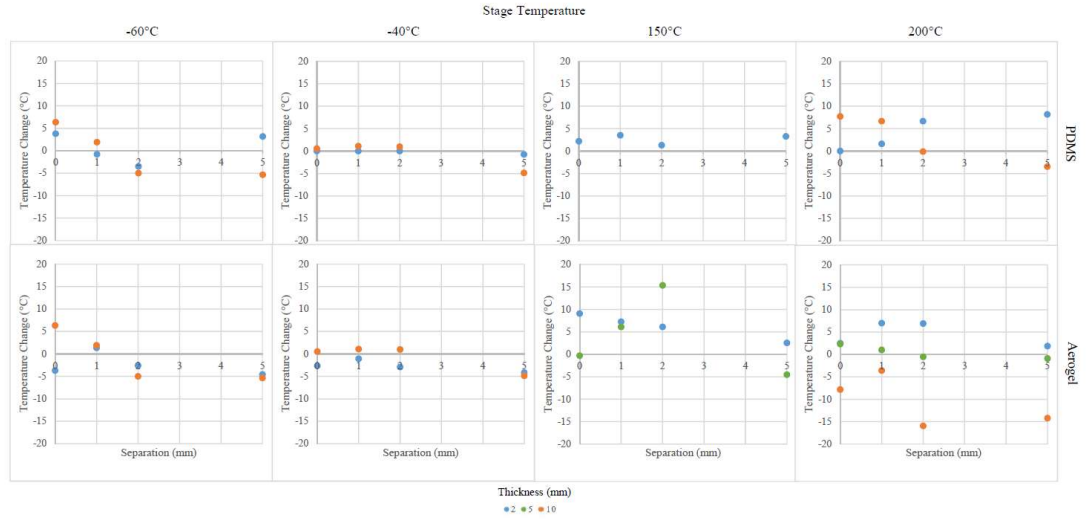
Figure 22: Luminescence results from measurements taken on non-crosslinked aerogel and PDMS samples constructed in Configuration 1: (a) decay times, (b) calculation surface temperatures of phosphor, (c) change in temperature on and off the fracture site.
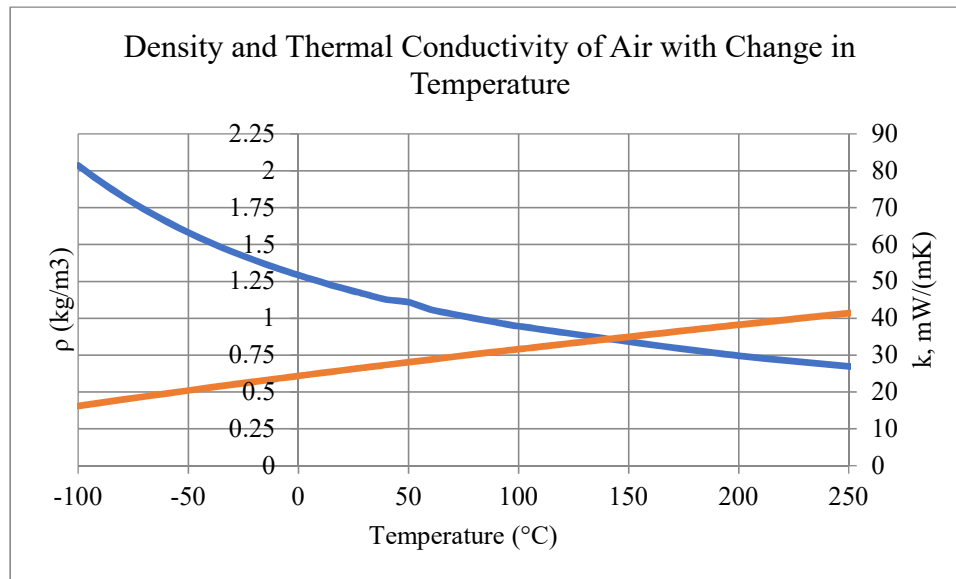
Figure 23: The change in density and thermal conductivity of air with respect to temperature (94). As the temperature increases, the density of the air decreases and the thermal conductivity increases. Both of these properties affect heat transfer through air.

Configuration 2: In this configuration a deliberate and defect, as previously defined, was created in the samples as in Section 3.4.1. Once more, the decay times were calculated

using the curve fitting to the decay emitted signals and are reported in Figure 24a. The corresponding temperatures were also calculated and are reported in Figure 24b. For PDMS, as the temperature increased and the sample surface got warmer, the decay time decreased. This trend was observed both above and below room temperature. For crosslinked aerogel, the decay time behavior followed a similar trend.

Measurements taken at 25°C, 70°C, and 100°C were excluded from analysis due to the surface temperatures of the samples at these temperatures falling outside of the temperature dependence of this phosphor's decay time.

For PDMS at 200°C and 150°C, a positive ΔT was detected which follows the same trend as 2 mm PDMS in the form of Configuration 1. This indicates that at the location of the fracture, the surface of the PDMS was better insulated with the introduction of air into the system. At -40°C and -60°C, a negative ΔT was measured, still indicating a more insulated sample surface at the fracture where the surface temperature was warmer than the remaining material surface. The thermal expansion of PDMS ($\alpha = 0.0003/°C$), as shown in Figure 25 (20), was considered as an effect on the defect size with change in temperature. It was determined that the thermal expansion had a negligible effect on the heat transfer through PDMS. These results suggest that thermographic phosphor could detect structural damage in the PDMS across a range of temperatures at a resolution of damage less than material failure.

For aerogel, across all four stage temperatures, the measured ΔT was positive in each case. Coupled with the results of 2 mm thick aerogel sample measured in the form of Configuration 1, which did not indicate a strong temperature dependence with

complete material failure of increasing fracture width, it can be suggested that the results from aerogel are inconclusive. Again, the thermal expansion of aerogel (published values proportional to $10^{-6}/°C$ (95)) was considered as an effect on the defect size and heat transfer and determined to have negligible effect. Further work should be done to explore this method with aerogel in this and other temperature ranges to determine the limits of phosphor thermometry in this application.

Overall, this data suggests that thermographic phosphor is a viable sensing mechanism to a resolution relevant to sensing structural damage before material failure because a detectable temperature change above noise level was demonstrated in a preliminary investigation. However, the specific limitations of the method are not confirmed by this study.
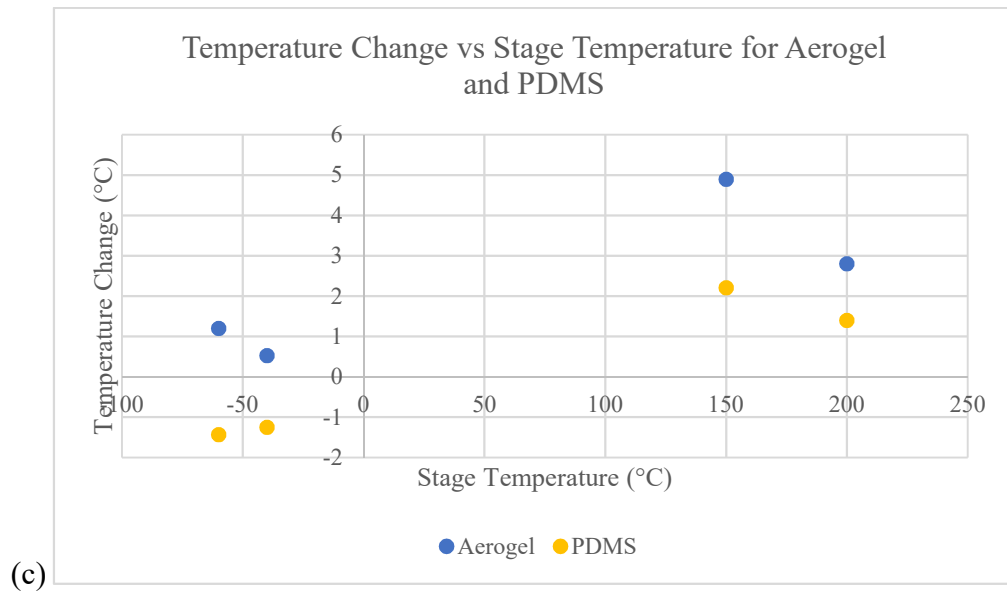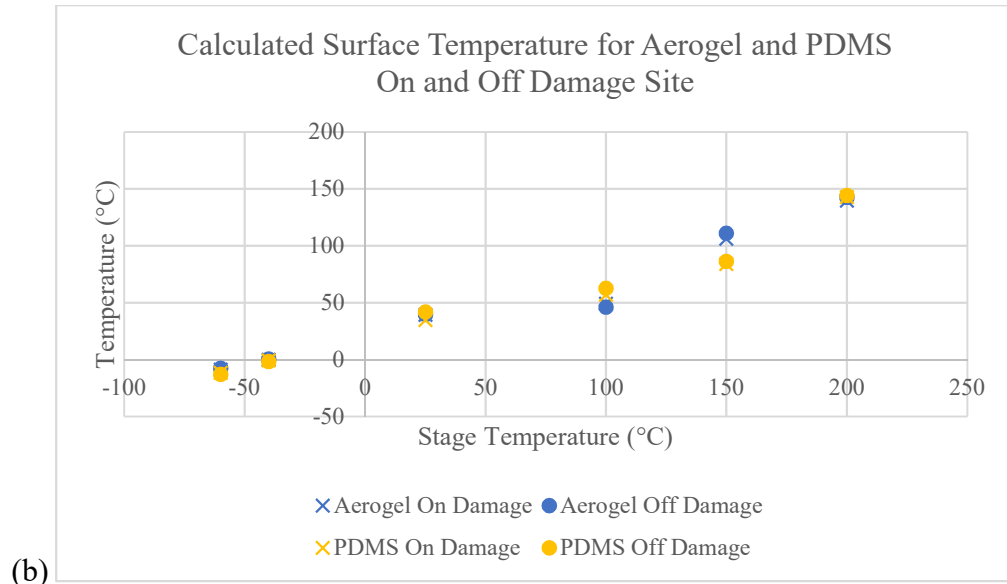

(a)

(b)

(c)
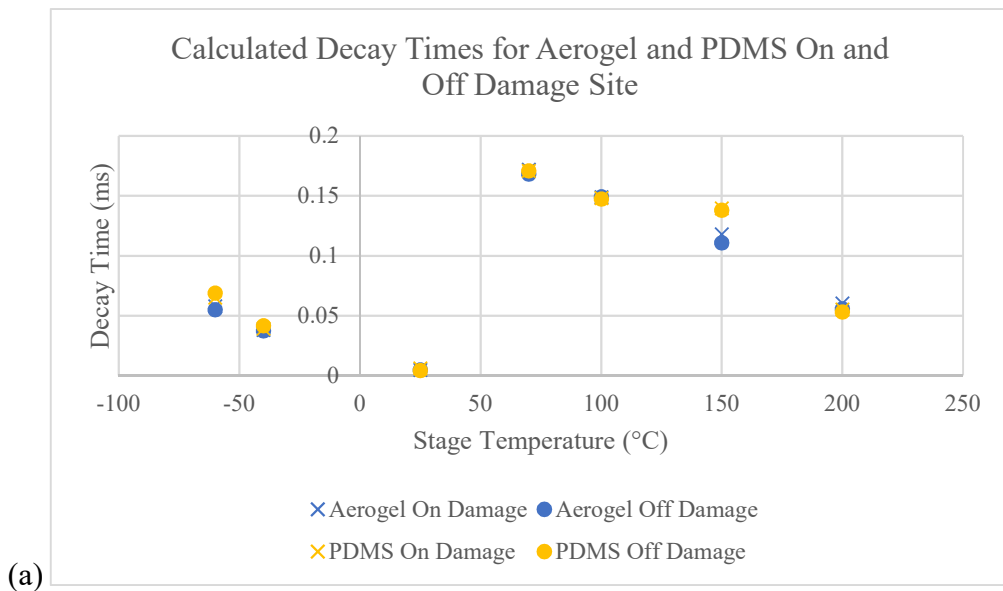
Figure 24: Luminescence results from measurements taken on samples constructed in Configuration 2: (a) decay times, (b) calculation surface temperatures of phosphor, (c) change in temperature on and off the fracture site.

71
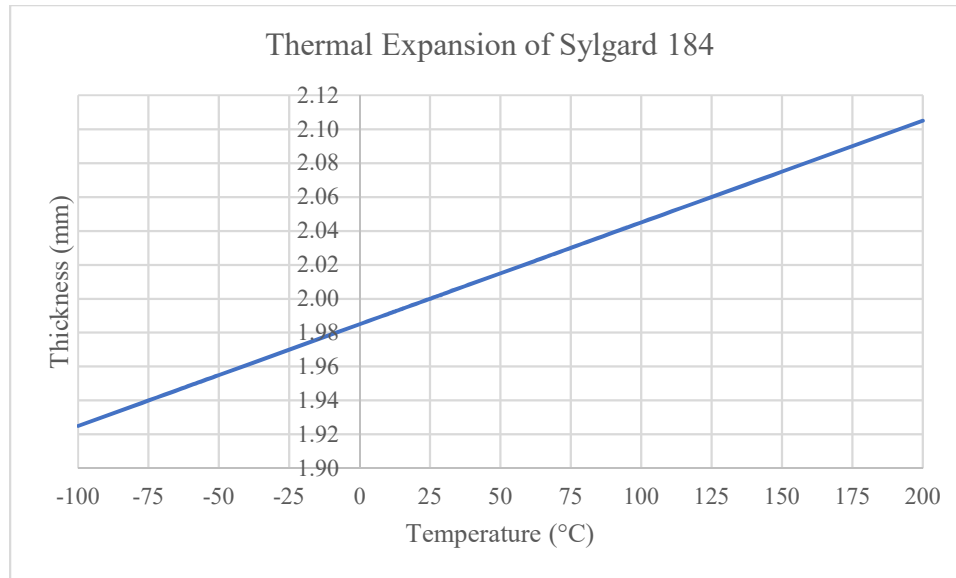
Figure 25: Thermal expansion of Sylgard 184 based on a linear thermal expansion coefficient of 0.0003/°C (20) where the 25°C thickness was 2 mm.

Chapter 6

Summary, Conclusion, and Future Work

6.1 Summary

In this study, the viability of using thermographic phosphor to detect structural damage in silica aerogel and PDMS was investigated. Phosphor powder was successfully introduced into aerogel synthesis as a discretely embedded layer. It was determined that the aerogel synthesis and drying process did not damage the phosphor and the compounds used in this study continue to perform as expected. To assess the viability of structural damage detection, two configurations were tested, and the results are summarized below:

Configuration 1: In general, for the thinner samples the change in temperature was detectable and clearly identified a material defect. As the thickness of the sample increased, the ΔT detected appeared to less and less noticeable. This was attributed to the better insulative behavior of the material. For 2 mm thick PDMS at 200°C, a trend of increasing ΔT with increase in fracture width was shown, indicating that the phosphor could detect a resolution of material failure up to a 5 mm fracture width. For aerogel of 2 mm thickness, a strong temperature dependence was not detected, indicating the aerogel insulated the phosphor on the sample surface better than the PDMS. For the remaining samples, weak or no temperature dependence on gap width was detected. As a result, further work was required to investigate the limitations of this method.

Configuration 2: For PDMS prepared in the manner of Configuration 2, changes in temperature between on gap and off gap were detectable at stage temperatures of -60°C, -40°C, 150°C, and 200°C. At stage temperatures of 25°C, 70°C, and 100°C the phosphor used did not show a strong temperature dependence behavior. This trend was also present for the aerogel sample. Based on this, it was determined that the thermographic phosphor could detect fracture in both aerogel and PDMS to a resolution below full material failure for certain temperature ranges.

6.2 Conclusion

Thermographic phosphor powders were successfully incorporated at discrete levels and superficially in aerogels and in PDMS materials and as a result can be used as means to interrogate the bulk of the material. Phosphor thermometry proved to be a viable option for remotely identifying structural defects in these two materials, with limitations. The changes in the thermal profile of the material as a result of material defects were used to infer information about the structural health of the material. Further work will be required to improve the resolution of this technique.

6.3 Future Recommendations

For future work, more detailed experiments following synthesis Method 1 are recommended. The failure-related luminescence experiments described in Chapter 5 were only performed with a phosphor layer deposited on the external face of the sample. Due to time limitations, in this investigation, it was not possible to test aerogel samples which had an embedded phosphor layer before/after damage. Also, it is recommended that other forms of material damage should be explored. In this investigation, only fracture resulting from mechanical loading was studied. Damage induced due to exposure to ionizing

radiation and thermal cycling, among others, was not evaluated. These types of material damage are particularly important for aerospace applications.

Another recommendation for future work is choosing a phosphor compound that has temperature dependent decay behaviors detectable over a wider range of temperatures than those studied here. It would also be beneficial to reduce the particle size of the phosphor powders by several orders of magnitude. This would significantly improve the outcome of the synthesis steps while also reducing the overall weight while improving the overall sensitivity of the composite. Computational modeling could also provide an advantage to exploring using this methodology in more than one dimension.

References

1. Meador, M. (2011). *Aerogels handbook.* Aegerter, M., et al. (Eds.) Springer Science & Business Media.

2. Sabri, F., et al. (2011). Spectroscopic evaluation of polyurea crosslinked aerogels, as a substitute for RTV-based chromatic calibration targets for spacecraft. *Advances in Space Research, 47*(3), 419-427. doi: 10.1016/j.asr.2010.09.014.

3. Flynn, G. (2014). Stardust interstellar preliminary examination; VII, Synchrotron x-ray fluorescence analysis of six Startdust Interstellar candidates measured with Advanced Photon Source 2-ID-D microphobe. *Meteoritics & Planetary Science, 49*(9), pp. 1626-1644. doi: 10.1111/maps.12144.

4. Tsou, P. (1995). Section 6. Commercialization and applications: Silica aerogel captures cosmic dust intact. *Journal of Non-Crystalline Solids, 186,* pp. 415-427. doi: 10.1016/0022-3093(95)00065-8.

5. Zrim, P., et al. (2015). Properties of laminated silica aerogel fibrous matting composites for footwear applications. *Textile Research Journal, 86*(10), p. 1063. doi: 10.1177/0040517515591781.

6. Baetens, R., et al. (2011). Review: Aerogel insulation for building applications: A state-of-the-art review. *Energy & Buildings, 43*(4), pp. 761-769. doi: 10.1016/j.enbuild.2010.12.012.

7. Maleki, H., et al. (2016). Synthesis and biomedical aplications of aerogels: Possibilities and challenges. *Advances in Colloid and Interface Science, 236*, pp. 1-27. doi: 10.1016/j.cis.2016.05.011.

8. Smith, D., et al. (1998). Aerogel-based thermal insulation. *Journal of Non-Crystalline Solids, 225*(1), p. 254. doi: 10.1016/S0022-3093(98)00125-2.

9. He, Ya-Ling and Tao Xie. (2015). Advances of thermal conductivity models of nanoscale silica aerogel insulation material. *Applied Thermal Engineering, 81,* pp. 28-50. doi: 10.1016/j.applthermaleng.2015.02.013.

10. Huang, D., et al. (2017). Characteristics of nanoporous silica aerogel under high temperature from 950°C to 1200°C. *Materials & Design, 129,* pp. 82-90. doi: 10.1016/j.matdes.2017.05.024.

11. Gurav, J., et al. (2010). Silica aerogel: Synthesis and applications. *Journal of Nanomaterials, 2010,* p. 11. doi: 10.1155/2010/409310.

12. Maleki, H., et al. (2014). An overview on silica aerogels synthesis and different mechanical reinforcing strategies. *Journal of Non-Crystalline Solids, 385,* pp. 55-74. doi: 10.1016/j.jnoncrysol.2013.10.017.

13. Lippi, G. and C. Mattiuzzi. (2016). Biological samples transporation by drones: ready for prime time? *Ann Transl Med, 4*(5), p. 92. doi: 10.21037/atm.2016.02.03.

14. Sabri, F., et al. (2013). Thermal conductivity studies of a polyurea cross-linked silica aerogel-RTV 655 compound for cryogenic propellant tank applications in space. *Acta Astronautica, 91,* pp. 173-179. doi: 10.1016/j.actaastro.2013.06.001.

15. Sabri, F., et al. (2014). Effect of aerogel particle concentration on mechanical behavior of impregnated RTV 655 compound material for aerospace applications. *Advances in Materials Science and Engineering, 2014,* pp. 1-10. doi: 10.1155/2014/716356.

16. Sabri, F., et al. (2013). In vivo ultrasonic detection of polyurea crosslinked silica aerogel implants. *PLoS ONE, 8*(6), pp. 1-8. doi: 10.1371/journal.pone.0066348.

17. Sabri, F., et al. (2012). Histological evaluation of the biocompatibility of polyurea crosslinked silica aerogel implants in a rat model: a pilot study. *PLoS ONE, 7*(12), pp. 1-7. doi: 10.1371/journal.pone.0050686.

18. Fontenot, R., et al. (2016). Mechanical, spectral, and luminescence properties of ZnS:Mn doped PDMS. *Journal of Luminescence, 170,* pp. 194-199. doi: 10.1016/j.jlumin.2015.10.047.

19. Sabri, F., et al. (2015). Polymer-encapsulated phosphor particles for in vivo phosphor luminescence applications. *International Journal of Polymeric Materials, 64*(13), pp. 690-694. doi: 10.1080/00914037.2014.1002096.

20. Dow Corning. *Sylgard 184 Silicone Elastomer Product Information.*

21. Wolf, M., et al. (2018). PDMS with designer functionalities -- Properties, modifications, strategies, and applications. *Progress in Polymer Science, 83,* pp. 97-134. doi: 10.1016/j.progpolymsci.2018.06.001.

22. Rajitha, G. and R. Dash. (2018). Optically transparent and high dielectric constant reduced graphene oxide (RGO)-PDMS based flexible composite for wearable and flexible sensors. *Sensors & Actuators, 277,* pp. 26-34. doi: 10.1016/j.sna.2018.04.040.

23. Allison, S., et al. (2015). In vivo x-ray imaging of phosphor-doped PDMS and phosphor-doped aerogel biomaterials. *International Journal of Polymeric Materials, 64*(16), pp. 823-830. doi: 10.1080/00914037.2015.1030652.

24. Roylance, D. (2001). *Introduction to fracture mechanics.* Department of Materials Science and Engineering, Massachusetts Institute of Technology. Cambridge, MA.

25. Campbell, F. C. (2012). *Mechanical behavior fatigue and fracture: understanding the basics. Vol 2.* (pp. 41-43). Materials Park: ASM International.

26. Poulain, X., et al. (2017). Damage in elastomers: nucleation and growth of cavities, micro-cracks, and macro-cracks. *Int J Fract, 205,* pp. 1-21. doi: 10.1007/s10704-016-0176-9.

27. Gu, J. and P. Chen. (2018). A failure criterion for homogeneous and isotropic materials distinguishing the different effects of hydrostatis tension and compression. *European Journal of Mechanics-A/Solids, 70*, pp. 15-22. doi: 10.1016/j.euromechsol.2018.01.013.

28. Craig, B. (2005). Material failure modes, part I: A brief tutorial on fracture, ductile failure, elastic deformation, creep, and fatigue. *Journal of Failure Analysis and Prevention, 5*(5), pp. 9-16. doi: 10.1361/154770205X70732.

29. Makris, R., et al. (2018). Crack luminescence as an innovative method for detection of fatigue damage. *Journal of Sensors and Sensor Systems, 7,* pp. 259-266. doi: 10.5194/jsss-7-259-2018.

30. Hasselman, D.P.H. (1978). Effect of cracks on thermal conductivity. *J. Composite Materials, 12*, pp. 403-407. doi: 10.1177/002199837801200405.

31. Mustafi, S., et al. (2008). Co-storage of cryogenic propellants for lunar exploration. *AIAA SPACE Conference & Exposition.* San Diego, CA: Cryogenics and Fluids Branch, NASA Goddard Space Flight Center. pp. 1-7.

32. Savin, A., et al. (2016). Damage detection of carbon reinforced composites using nondestructive evaluation with ultrasound and electromagnetic methods. *IOP Conferece Series: Materials Science & Engineering, 133*(1), p. 1. doi: 10.1088/1757-899X/133/1/012013.

33. Ould, S., et al. (2002). Detection of chemical damage in concrete using ultrasound. *Ultrasonics, 40*(1), pp. 247-251. doi: 10.1016/S0041-624X(02)00146-4.

34. Vogelaar, B. and M. Golombok. (2017). Simplified ultrasound damage detection in fluid-filled pipes. *Journal of Nondestructive Evaluation, 36,* p. 63. doi: 10.1007/s10921-017-0443-3.

35. Zumpano, G. and M. Meo. (2006). A new damage detection technique based on wave propagation for rails. *International Journal of Solids and Structures, 43*(5), pp. 1023-1046. doi: 10.1016/j.ijsolstr.2005.05.006.

36. Yao, J. and G. Yu. (2017). Small-scale rail flaw detection car design and damage position estimation. *International Conference on Sensing, Diagnostics, Prognostics, and Control (SDPC).* Shanghai, China: IEEE. doi: 10.1109/SDPC.2017.20.

37. Mitchell, K., et al. (2016). Synthesis and characterization of flexible thermographic phosphor temperature sensors. *Optical Materials, 60,* pp. 50-56. doi: 10.1016/j.optmat.2016.06.039.

38. Rodriguez, S., et al. (2018). Accelerated thermal profiling of gas turbine components using luminescent thermal history paints. *Journal of the Global Power and Propulsion Society, 2.* doi: 10.22261/JGPPS.S3KTGK.

39. Michalski, L., et al. (2001) Automatic Pyrometers. Temperature Measurement, Second Edition. *Automatic Pyrometers* (pp. 177-208). John Wiley & Sons, Ltd. doi: 10.1002/0470846135.

40. Gillespie, P., et al. (2016). A bias compensated cross-relation approach to thermocouple characterisation. *IFAC-PapersOnLine, 49*(5), pp. 43-48. doi: 10.1016/j.ifacol.2016.07.087.

41. Allison, S., et al. (2003). Advances in high temperature phosphor thermometry for aerospace applications. *39th AIAA/ASME/SAE/ASEE Joint Propulsion Conference and Exhibit.* p. 4584. doi: 10.2514/6.2003-4584.

42. Sami, A., et al. (1999). Mapping the surface temperature of ceramic and superalloy turbine engine components using laser-induced flurescence of thermographic phosphor. *Optics and Lasers in Engineering, 31*(5), pp. 354-351. doi: 10.1016/S0143-8166(99)00031-7.

43. Knappe, C. (2013). Phosphor thermometry on surfaces. *Lund Reports on Combustion Physics* doi: lup.lub.lu.se/record/4022201.

44. Parajuli, P., et al. (2017). Spincoat-fabricated multilayer PDMS-phosphor composites for thermometry. *Measurement Science and Technology, 28*(6). doi: 10.1088/1361-6501/aa63be.

45. Eldridge, J., et al. (2004). Depth-penetrating temperature measurements of thermal barrier coatings incorporating thermographic phosphors. *Journal of Thermal Spray Technology, 13*(1), pp. 44-50. doi: 10.1007/s11666-004-0048-0.

46. Allison, S., et al. (1989). Rare-earth phosphors for remote thermographic applications. Applied Technology Division, Oak Ridge National Lab., TN (USA). No. ORNL/ATD-12.

47. O'Connell, J. and J. Haile. (2005). *Thermodynamics: fundamentals for applications.* Cambridge University Press. doi: 10.3390/s8095673.

48. Rohsenow, W. and C. Young. (1998). *Handbook of heat transfer, Vol. 3.* J. Hartnett (Ed.). New York: McGraw-Hill.

49. Yang, S. and W. Tao. *Heat Transfer, Edition 4.* (2006). Beijing: Higher Eduation Press.

50. Good, B. (2005). Structure and thermal conductivity of silica aerogels from computer simulations. *MRS Proceedings, 885.* doi: 10.1557/PROC-0885-A09-35.

51. Warrier, P., et al. (2010). Heat transfer in nanoparticle suspensions: modeling the thermal conductivity of nanofluids. *AlChE Journal, 56*(12), pp. 3243-3256. doi: 10.1002/aic.12228.

52. Bi, C. and G. Tang. (2013). Effective thermal conductivity of the solid backbone of aerogel. *International Journal of Heat and Mass Transfer, 64,* pp. 452-456. doi: 10.1016/j.ijheatmasstransfer.2013.04.053.

53. Zeng, S., et al. (1995). Theoretical modeling of carbon content to minimize heat transfer in silica aerogel. *Journal of Non-Crystalline Solids, 186,* pp. 271-277. doi: 10.1016/0022-3093(95)00076-3.

54. Lienhard, J. *A heat transfer textbook, 4th edition*. (2017). Dover Publications.

55. Dixon, C., et al. (2000). Transient plane source technique for measuring thermal properties of silicone materials used in electronic assemblies. *The International Journal of Microcircuits and Electronic Packaging, 23,* pp. 494-500.

56. Lui, H., et al. (2017). Experimental investigations on temperature dependent effective thermal conductivity of nanoporous silica aerogel composite. *Experimental Thermal and Fluid Science, 84*, pp. 67-77. doi: 10.1016/j.expthermflusci.2017.01.021.

57. Bouguerra, A., et al. (2001). Measurement of thermal conductivity, thermal diffusivity and heat capacity of highly porous building materials using transient plane source technique. *International Communications in Heat and Mass Transfer, 28*, pp. 1065-1078. doi: 10.1016/S0735-1933(01)00310-4.

58. Zhao, D., et al. (2016). Measurement techniques for thermal conductivity and interfacial thermal conductance of bulk and thin film materials. *Journal of Electronic Packaging, 138*, pp. 40802-40819. doi: 10.1115/1.4034605.

59. Therm Test, Inc. (2014). *Hot disk thermal constants analyser instruction manual.* Fredericton, NB.

60. Krupa, P. and S. Malinaric. (2014). Using the transient plane source method for measuring thermal parameters of electroceramics. *Int. J. Math., Comput., Statistical, Natural Phys. Eng, 8*, pp. 733-738.

61. Tritt, T. (Ed.). (2005). Thermal conductivity: theory, properties, and applications. Springer Science & Business Media.

62. Lee, H., et al. (2017). Derivation of complete stress-strain curve for SSTT-confined high-strength concrete in compression. *Journal of Testing and Evaluation, 46*, pp. 1-10. doi: 10.1520/JTE20160195.

63. Ronda, C. (2007). *Luminescence: from theory to applications.* John Wiley & Sons.

64. Shionoya, S., et al. (Eds.) (2006). *Phosphor handbook.* CRC Press.

65. Virk, H., (Ed.). (2015). *Luminescent materials and their applications.* Trans Tech Publications.

66. Khalid, A. and K. Kontis. (2008). Thermographic phosphors for high temperature measurements: principles, current state of the art, and recent applications. *Sensors, Vol. 8*(9), pp. 5673-5744. doi: 10.3390/s8095673.

67. Yap, S., et al. (2009). Temperature dependent characteristics of La2O2S: Ln [Ln=Eu, Tb] with various Ln concentrations over 5–60°C. *Journal of Luminescence, 129*(5), pp. 416-422. doi: 10.1016/j.jlumin.2008.10.019.

68. Pringsheim, P. (1949). *Fluorescence and phosphorescence.* New York: Interscience.

69. Allison, S. and G. Gillies. (1997). Remote thermometry with thermographic phosphors: Instrumentation and applications. *Review of Scientific Instruments, 68*(7), pp. 2615-2650. doi: 10.1063/1.1148174.

70. Beran, A. and E. Libowitzky. (2004). *Spectroscopic methods in mineralogy.* The Mineralogical Society of Great Britain and Ireland.

71. Valeur, B. and J. Brochon. (Eds.). (2012). New trends in fluorescence spectroscopy: applications to chemical and life sciences. *Spring Science & Business Media, Edition 1.* doi: 10.1007/978-3-642-56853-4.

72. Lorad Chemical Corporation. (2018). *Safety Data Sheet: La2O2S.*

73. Riuttamaki, T. (2011). Upconverting phosphor technology: exceptional photoluminescent properties light up homogeneous bioanalytical assays.

74. Allison, S. and M. Cates. Phosphor thermometry tutorial. Oak Ridge National Lab., U.S. Dept. of Energy.

75. Collins, S., et al. (1998). Comparison of fluorescence-based temperature sensor schemes: theoretical analysis and experimental validation. *Journal of Applied Physics, 84*(9), pp. 4649-4654. doi: 10.1063/1.368705.

76. Cates, M., et al. (1997). Phosphor thermometry at cryogenic temperatures. *Review of Scientific Instruments, 68*(6), pp. 2412-2417. doi: 10.1063/1.1148125.

77. Demas, J. and C. Glenn. (1970). Photoluminescence decay curves: an analysis of the effects of flash duraction and linear instrumental distorations. *Analytical Chemistry, 42*(9), pp. 1010-1017. doi: 10.1021/ac60291a035.

78. Allison, S. (2018). Interview.

79. Hecht, E. (1998). *Optics, 4th Edition.* Addison Wesley Longman Inc.

80. Evangelisti, F., et al. (1974). Dependence of exciton reflectance on field and other surface characteristics: The case of InP. *Physical Review B, 9*(4), p. 1516. doi: 10.1103/PhysRevB.9.1516.

81. Owen, T. (1996). *Fundamentals of UV-visible spectroscopy: a primer.* Hewlett-Packard.

82. Tams, C. and N. Enjalbert. (2009). *The use of UV/Vis/NIR spectroscopy in the development of photovoltaic cells.* Perkin Elmer Inc. Waltham, MA.

83. Kirk, J. (1994). *Light and photosynthesis in aquatic ecosystems.* Cambridge Univerity Press. p. 15.

84. Berdnik, V. (2005). Reconstruction of the characteristics of a light-scattering layer from its reflectance and transmittance: The neural network method. *Optics and Spectroscopy, 99*(1), pp. 98-105. doi: 10.1134/1.1999900.

85. Kuhta, N., et al. (2011). Asymmetric reflectance and cluster size effects in silver percolation films. *Physical Review B, 84*(16), p. 165130. doi: 10.1103/PhysRevB.84.165130.

86. Hunt, A. and M. Ayers. (1998). Light scattering studies of UV-catalyzed gel and aerogel structure. *Journal of Non-Crystalline Solids, 225*, pp. 325-329. doi: 10.1016/S0022-3093(98)00132-X.

87. Bohren, C. and D. Huffman. (2008). *Absorption and scattering of light by small particles.* John Wiley & Sons.

88. Zhao, L., et al. (2016). Modeling silica aerogel optical performance by determing its radiative properties. *AIP Advances, 6*(2), p. 025123. doi: 10.1063/1.4943215.

89. Chemistry LibreTexts: Phase Diagrams. (2017). *Chemistry LibreTexts.*

90. In, E. and H. Naguib. (2015). Fabrication and characterization of silica aerogel as synthetic tissues for medical imaging phantoms. *AIP Conference Proceedings, 1664*(1), p. 130002. doi: 10.1063/1.4918495.

91. Gesser, H. and P. Goswami. (1989). Aerogels and related porous materials. *Chemical Reviews, 89*(4), pp. 765-788. doi: 10.1021/cr00094a003.

92. Dorcheh, A. and M. Abbasi. (2008). Silica aerogel: synthesis, properties and characterization. *Journal of Materials Processing Technology, 199*, pp. 10-26. doi: 10.1016/j.jmatprotec.2007.10.060.

93. Parajuli, P. (2017). Exploration of thin film polymers for phosphor thermometry. Thesis, University of Memphis.

94. Diehl, W. (1962). *Report No. 218: Standard atmosphere - tables and data.* Bureau of Aeronautics, Navy Department.

95. Allison, S., et al. (2017). In vivo x-ray excited optical luminescence from phosphor-doped aerogel and Sylgard 184 composites. *Radiation Physics and Chemistry, 135,* pp. 88-93. doi: 10.1016/j.radphyschem.2017.01.045.

96. Gross, J. and J. Fricke. (1995). Thermal expansion of carbon and silica aerogels above room temperature. *Journal of Non-Crystalline Solids, 186*(2), pp. 301-308. doi: 10.1016/0022-3093(95)00053-4.